APPENDIX A

United States Application Serial No. 10/687,371

SYSTEMS AND METHODS FOR GEOPHYSICAL IMAGING USING AMORPHOUS COMPUTATIONAL PROCESSING

GEOPHYSICS, VOL. 53, NO. 12 (DECEMBER 1988); P. 1540–1546, 8 FIGS.

Paraxial ray Kirchhoff migration

T. H. Keho* and W. B. Beydoun*

ABSTRACT

A rapid nonrecursive prestack Kirchhoff migration is implemented (for 2-D or 2.5-D media) by computing the Green's functions (both traveltimes and amplitudes) in variable velocity media with the paraxial ray method. Since the paraxial ray method allows the Green's functions to be determined at points which do not lie on the ray, two-point ray tracing is not required. The Green's functions between a source or receiver location and a dense grid of thousands of image points can be estimated to a desired accuracy by shooting a sufficiently dense fan of rays.

For a given grid of image points, the paraxial ray method reduces computation time by one order of magnitude compared with interpolation schemes.

The method is illustrated using synthetic data generated by acoustic ray tracing. Application to VSP data collected in a borehole adjacent to a reef in Michigan produces an image that clearly shows the location of the reef.

INTRODUCTION

Kirchhoff migration is an integral technique that back-propagates a wave field. This procedure, when applied to an observed scattered wave field, focuses the field at the locations in the medium from which it was scattered, thus producing an image of the medium. Among those who introduced the Kirchhoff integral to exploration geophysics for imaging the earth were Gardner et al. (1974), French (1974, 1975), and Schneider (1978). The technique was developed for application to surface seismic recording geometries and constant-velocity media and, subsequently, was adapted to quasi-layered velocity structures by sequentially applying constant-velocity migration for each layer and back-propagating the scattered field downward to the top of the next layer (Berryhill, 1979). This procedure is known as recursive migration (e.g., Berkhout, 1982).

In general, for two-dimensional (2-D) velocity variations, one cannot apply a recursive migration using the constant-velocity Green's functions; a nonrecursive migration must be employed with the Green's functions determined numerically, for example, by ray tracing. One recording geometry that requires the use of numerically computed Green's functions is the Vertical Seismic Profile (VSP). Since velocity varies with depth, the velocity changes across the receiver array in a manner equivalent to lateral velocity variation for surface seismic experiments. Such nonrecursive implementations of Kirchhoff migration are computationally expensive except for special cases. Carter and Frazer (1984) developed a fast, nonrecursive Kirchhoff integral technique based upon Fermat's principle for the case of smooth lateral velocity variations.

The goal of this paper is to describe a fast, nonrecursive prestack Kirchhoff migration for variable velocity media with large lateral velocity variations, applicable for 2-D or 2.5-D acoustic or elastic media, by computing the Green's functions with the paraxial ray method. First, we give a brief review of Kirchhoff migration which describes how to back-propagate the wave field and form an image of the medium. Second, we follow with a brief description of the paraxial ray method. Third, we use the concept of reciprocity to implement Kirchhoff migration with variable velocity using the paraxial ray method. The method is illustrated with synthetic VSP data and with VSP data collected in a borehole adjacent to a reef in Michigan.

KIRCHHOFF MIGRATION

In this section we briefly review Kirchhoff migration and define an imaging condition for 2-D acoustic media. The final result, however, is a general form that is adaptable to 2-D or 2.5-D acoustic or elastic media.

The Rayleigh II integral (Berkhout, 1982) describes how to forward propagate the acoustic pressure field from a surface

Manuscript received by the Editor May 11, 1987; revised manuscript received May 16, 1988.
*Formerly Department of Earth, Atmospheric and Planetary Sciences, MIT; presently ARCO Oil and Gas Company, 2300 West Plano Parkway, PRC-2037, Plano, TX 75075.

s to a point $\mathbf{r}$,

$$P(\mathbf{r}, \omega) = \frac{1}{2\pi} \int_s P(\mathbf{r}_g, \omega) \nabla G(\mathbf{r}_g | \mathbf{r}, \omega) \cdot \hat{\mathbf{n}}\, ds, \tag{1}$$

where $P(\mathbf{r}, \omega)$ is the temporal Fourier transform of the pressure field at the point $\mathbf{r}$, $P(\mathbf{r}_g, \omega)$ is the temporal Fourier transform of the pressure field on the recording surface s at the geophone location $\mathbf{r}_g$, ds is a function of $\mathbf{r}_g$, $G(\mathbf{r}_g | \mathbf{r}, \omega)$ is the Green's function from point $\mathbf{r}$ to point $\mathbf{r}_g$, and $\hat{\mathbf{n}}$ is the inward unit vector normal to the surface.

Migration requires propagation of the field backward into the medium where the field will focus at the scatterers and form an image of the medium. The back-propagated field can be expressed as

$$P(\mathbf{r}, \omega) = \frac{1}{2\pi} \int_s P(\mathbf{r}_g, \omega) \nabla G^*(\mathbf{r}_g | \mathbf{r}, \omega) \cdot \hat{\mathbf{n}}\, ds, \tag{2}$$

where $G^*(\mathbf{r}_g | \mathbf{r}, \omega)$ is the complex conjugate of the Green's function $G(\mathbf{r}_g | \mathbf{r}, \omega)$.

A function $R(\mathbf{r}, \omega)$ is defined as the ratio of the back-propagated field from the receivers $P(\mathbf{r}, \omega)$ to the incident field from the source $P_{\text{src}}(\mathbf{r}, \omega)$ (e.g., Claerbout, 1970);

$$R(\mathbf{r}, \omega) \equiv \frac{P(\mathbf{r}, \omega)}{P_{\text{src}}(\mathbf{r}, \omega)}. \tag{3}$$

The synthetically determined incident field $P_{\text{src}}(\mathbf{r}, \omega)$ equals $S(\omega)G(\mathbf{r}_s | \mathbf{r}, \omega)$, $S(\omega)$ being the source function and $\mathbf{r}_s$ being the source location. Combining equations (2) and (3) gives the holographic (i.e., frequency-domain) form of Kirchhoff migration. A pseudoreflection coefficient can be determined from equation (3) in the time domain by setting $t = 0$. The term "pseudo" is used because the data are not due only to normally incident reflections. The assumption inherent in equation (3) is that point scatterers in the medium are excited at the arrival time of the incident wave from the source. This is referred to as the "excitation time imaging condition" (Chang and McMechan, 1986). The Green's functions are expressed in the form

$$G(\mathbf{r}_s | \mathbf{r}, \omega) \equiv A(\mathbf{r}_s | \mathbf{r}) \exp\left(i\omega\tau(\mathbf{r}_s | \mathbf{r})\right) \tag{4a}$$

and

$$G(\mathbf{r}_g | \mathbf{r}, \omega) \equiv A(\mathbf{r}_g | \mathbf{r}) \exp\left(i\omega\tau(\mathbf{r}_g | \mathbf{r})\right), \tag{4b}$$

where A and τ are ray amplitude and traveltime, respectively. The subscripts s and g designate shot and geophone. For the far-field case, one obtains the pseudoreflection coefficient,

$$R(\mathbf{r}) = \int_s W(\mathbf{r}_g, \mathbf{r}_s, \mathbf{r}) D(\mathbf{r}_g, \mathbf{r}_s, \mathbf{r})\, ds, \tag{5}$$

where the weighting function W and the data D are given by

$$W(\mathbf{r}_g, \mathbf{r}_s, \mathbf{r}) = -\frac{1}{2\pi c} \frac{A(\mathbf{r}_g | \mathbf{r})}{A(\mathbf{r}_s | \mathbf{r})} \cos\theta \tag{6}$$

and

$$D(\mathbf{r}_g, \mathbf{r}_s, \mathbf{r}) = \frac{\partial}{\partial t} P\left[\mathbf{r}_g, \tau(\mathbf{r}_s | \mathbf{r}) + \tau(\mathbf{r}_g | \mathbf{r})\right], \tag{7}$$

with θ being the angle between the normal to the surface s and ray $(\mathbf{r}_g | \mathbf{r})$.

Note that equation (5), which was derived for 2-D acoustic media, has been written in a general form. The weighting function W and the data D in equation (5) will be different, depending upon whether the imaging problem is 2-D, 2.5-D, acoustic, or elastic. For example, for 2-D elastic Kirchhoff migration, W will be a 2×2 matrix and D will be a two-component vector (Keho and Wu, 1987; Kuo and Dai, 1984). Also, instead of integrating along the recording surface ds, integration can be performed over the solid angle between the incoming and outgoing rays at the image point (Miller et al., 1984).

The weighting function W depends on the velocity structure. The implementation of equation (5) becomes expensive when the Green's functions [equation (4)] in W cannot be determined analytically.

THE PARAXIAL RAY METHOD

A fast migration scheme can be obtained by computing the Green's functions with the paraxial ray method. The method, developed by Beydoun (1985a), was presented for modeling by Beydoun (1985b) and applied to inverse scattering problems by Beydoun and Keho (1986). This method is an outgrowth of the work on Gaussian beams by Červený and his colleagues (e.g., Červený et al., 1982; Červený et al., 1984) and is described in detail by Beydoun and Keho (1987). The value of the paraxial ray method is its computational efficiency: the method does not require two-point ray tracing. Instead, the Green's function can be determined at any point which is near, in the paraxial sense, the desired ray (Beydoun and Keho, 1987).

The conditions for validity of ray methods are described by Ben-Menahem and Beydoun (1985), and for the paraxial ray method by Beydoun and Keho (1987). Where dynamic ray tracing is not valid, for example in regions of the model where caustics or diffractions occur, the paraxial ray method also will not be valid. Therefore, the velocity model used for migration should not contain such regions. We should also mention that the migration scheme we have described is not valid where the phase of the scattered wave field changes (e.g., due to postcritical reflections or caustics). This is true for nearly all migration methods. Therefore, we cannot benefit by using more sophisticated methods such as the Gaussian beam method for computing Green's functions in these complicated regions.

The Green's function for the acoustic field [the corresponding expressions for elastic media are given by Beydoun and Keho (1987)] at the point M' on the ray is given by

$$P(M', \omega) = A_0(M', \omega) \exp\left\{i\omega\tau(M')\right\}. \tag{8}$$

The Green's function at a point M which is near but not on the ray can be approximated by

$$P(M, \omega) = qA_0(M', \omega) \exp\left\{i\omega\left[\tau(M') + \frac{n^2 K_\omega}{2}\right]\right\}, \tag{9}$$

where q is an amplitude correction, which, for a point source, is given by

$$q = \left(1 + \frac{\delta R_\omega}{\sqrt{J^S}}\right)^{-1}; \tag{10}$$

δR_w is the distance from the wavefront as determined at M' to the point M off the ray, and J^S is the Jacobian of the transformation between Cartesian and ray-centered coordinates. The traveltime correction is given by the term $n^2K_w/2$, where K_w is the wavefront curvature at the point M' on the ray, and n is the perpendicular (to the ray) distance from the point M' on the ray to the point M near the ray. All of the quantities in equation (9) are readily available from standard dynamic ray tracing.

By shooting a fan of appropriately spaced rays, Green's functions can be determined rapidly between the origination of the fan and every other point in the medium. This is extremely valuable for migration, as well as for other inverse scattering problems such as variable velocity tomography or Born inversion [e.g., see computational requirements of Beylkin (1985) or Levy and Esmersoy (1987)] which require knowledge of Green's functions between the sources and all the points in the image area and between the receivers and all of the points in the image area. Typically, there are tens of thousands of image points and performing two-point ray tracing between each image point and each source or receiver would be prohibitively expensive.

IMPLEMENTATION

Implementation of Kirchhoff migration using the paraxial ray method was suggested by Keho (1984). Beydoun and Keho (1987) developed and tested the paraxial ray method for application to inverse scattering problems, i.e., computing Green's functions at a dense grid of points. Here, we implement prestack Kirchhoff migration with the paraxial ray method in order to achieve an accurate and less computationally expensive migration.

Computation time for prestack Kirchhoff migration in variable velocity media can be decreased by two orders of magnitude by invoking reciprocity—replacing $G(\mathbf{r}|\mathbf{r}_g, \omega)$ with $G(\mathbf{r}_g|\mathbf{r}, \omega)$ and $G(\mathbf{r}|\mathbf{r}_s, \omega)$ with $G(\mathbf{r}_s|\mathbf{r}, \omega)$ in equation (3), i.e., shooting from sources and receivers toward the image points, instead of shooting from image points to receivers and sources. Invoking reciprocity is a common procedure, e.g., see Hu and McMechan (1986) or Gray (1988).

Use of the paraxial ray method further reduces computation time by another order of magnitude compared with computing Green's functions (traveltimes and amplitudes) from a 2-D polynomial fitted to Green's functions determined at points along the rays. If only traveltimes are required, the reduction in computation time is less than one order of magnitude. Interpolation schemes (Hu and McMechan, 1986; Gray, 1988) such as polynomial fitting or spline or linear interpolation between rays will result in smooth traveltime and equal amplitude surfaces; however, smoothness is not an indication of accuracy. Interpolation schemes provide no information on how to control ray density in order to maintain accuracy for traveltimes and amplitudes. This lack of information usually results in more rays being shot than necessary. Unlike interpolation, the paraxial approximation is derived from the physics of wave propagation. Consequently, information is available which enables the user to control ray density interactively (Beydoun and Keho, 1987). In most cases, a single ray is sufficient to determine the Green's functions at hundreds of image points.

Since the data can be migrated one receiver at a time, with currently available field computing systems migration of VSP data can be performed as the data are recorded. The image array can be dumped at any time to look at the image as it is developing. Obviously, in such a situation, very little preprocessing can be done. In the examples that follow, however,

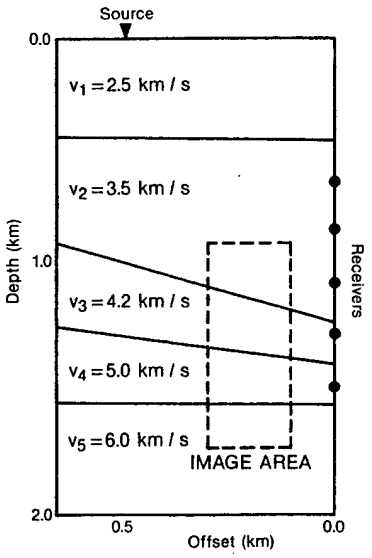

FIG. 1. Acoustic ray-tracing velocity model. There are 80 receivers on the line indicated by the five dots, and 4000 image points in the image area enclosed by the dashed rectangle.

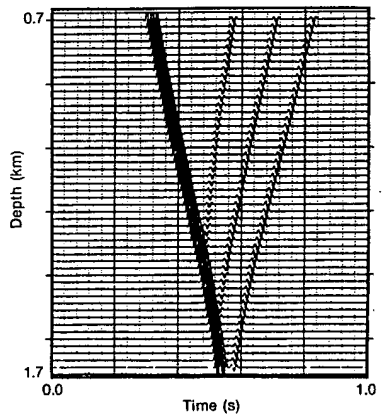

FIG. 2. Synthetic acoustic data generated by the paraxial ray method using the velocity model in Figure 1. The direct wave from the source and the primary reflection from each of the three interfaces in the image area are included.

very satisfactory images are obtained with minimal preprocessing.

EXAMPLES

In this section paraxial ray Kirchhoff migration (PRKM) is illustrated with a synthetic example and is applied to field data. The synthetic data example shows the results of migrating VSP data generated from a ray-tracing model consisting of several dipping layers, and illustrates the effects of low ray density. In the field data example, a reef in Michigan is imaged using multioffset VSP data. In both of these examples the incident part of the wave field (first downgoing arrival) was removed by filtering. In the field example, ringing traces were killed. No other processing was applied to the data.

Synthetic data example

The model consists of flat and dipping interfaces (Figure 1) with 80 receivers and 4000 image points. The acoustic synthetic data (Figure 2) contain the incident primary reflected field generated using the paraxial ray method. Figure 3 shows ray fans from the source and from one of the receivers. The ray fans in this figure are very sparse and are shown only for the purpose of illustrating how each ray captures image points that are near it in the paraxial sense.

Figure 4 shows the migrated data that result from using exact velocities and a fan of rays that are mildly sparse, i.e.,

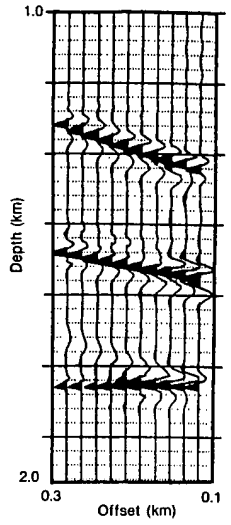

FIG. 4. Migration of the synthetic data in Figure 2 using the exact velocities. This figure illustrates the result of migration with a mildly sparse fan of rays (a few percent of the image points are missed by each ray fan). Notice the choppy look of the image. Parts of the waveform in the image are zero due to those image points being missed by the ray fan from the source. This is easily corrected by shooting a denser fan of rays.

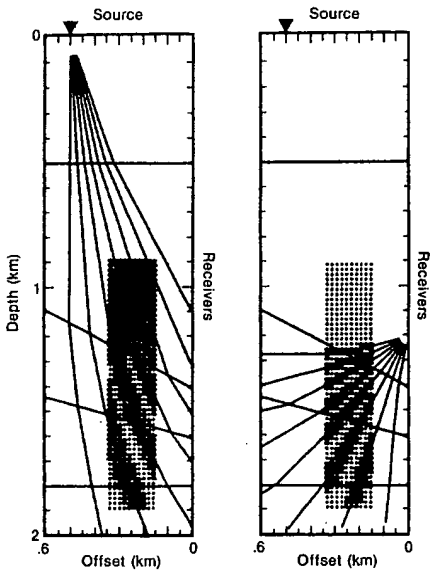

FIG. 3. Example of a fan of rays shot from the source (left) and from one of the 80 receivers (right). The small dots indicate image points. The large dots indicate the image points each ray captured (i.e., for which the Green's function was determined).

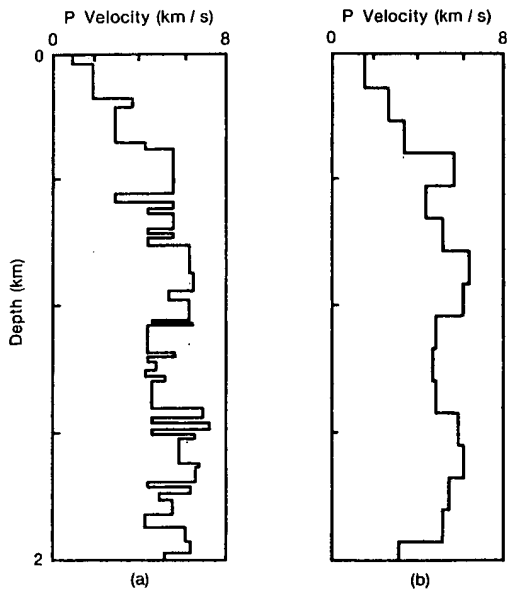

FIG. 5. (a) *P*-wave velocity structure at the VSP site in Manistee County, Michigan determined from well logs and 1-D iterative VSP waveform inversion, (b) low-pass filtered version of (a) used as the migration velocity.

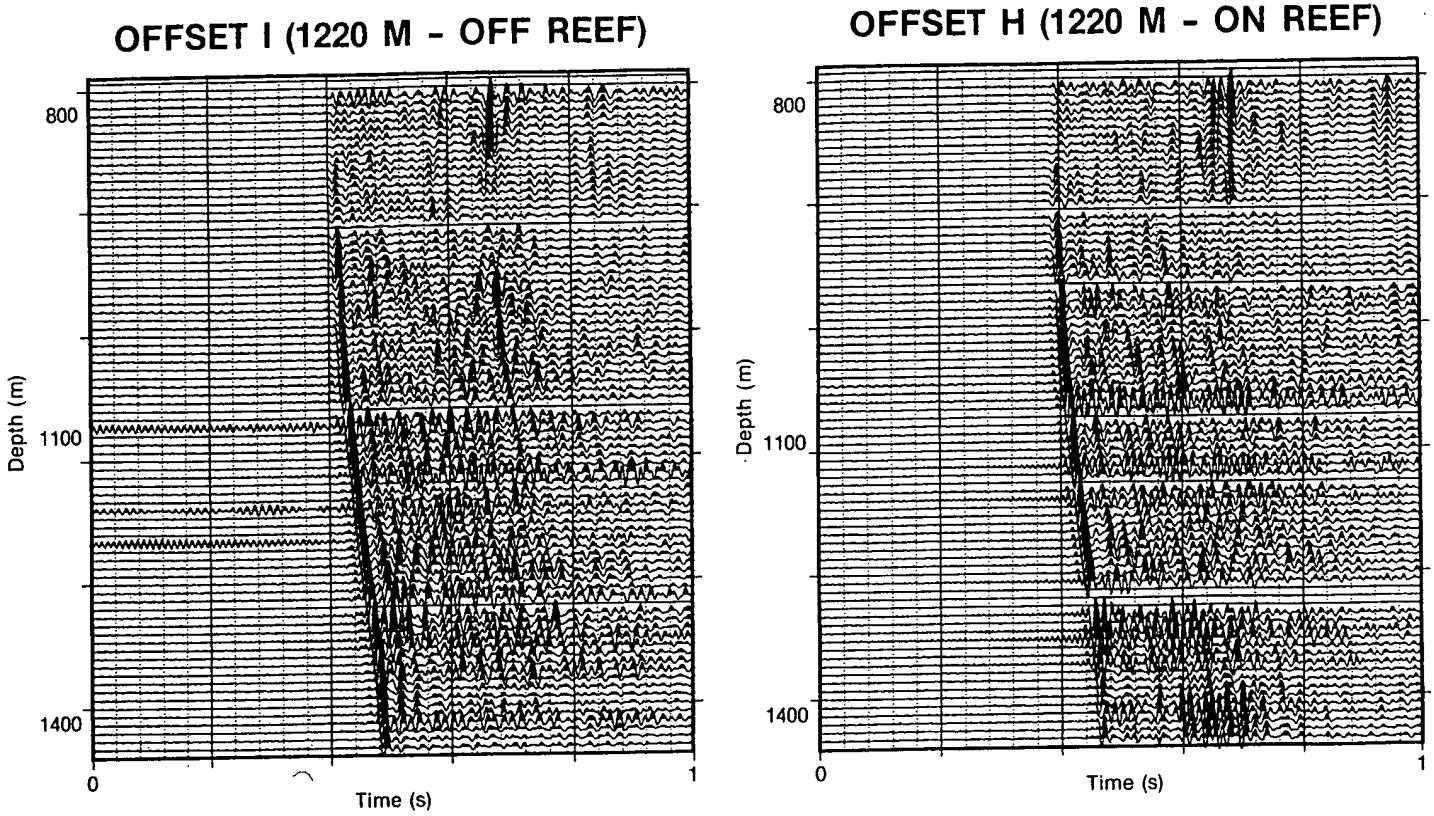

FIG. 6. Vertical component field data from offset I (off reef) and offset H (on reef). Notice the reflection from the reef area near 1400 m.

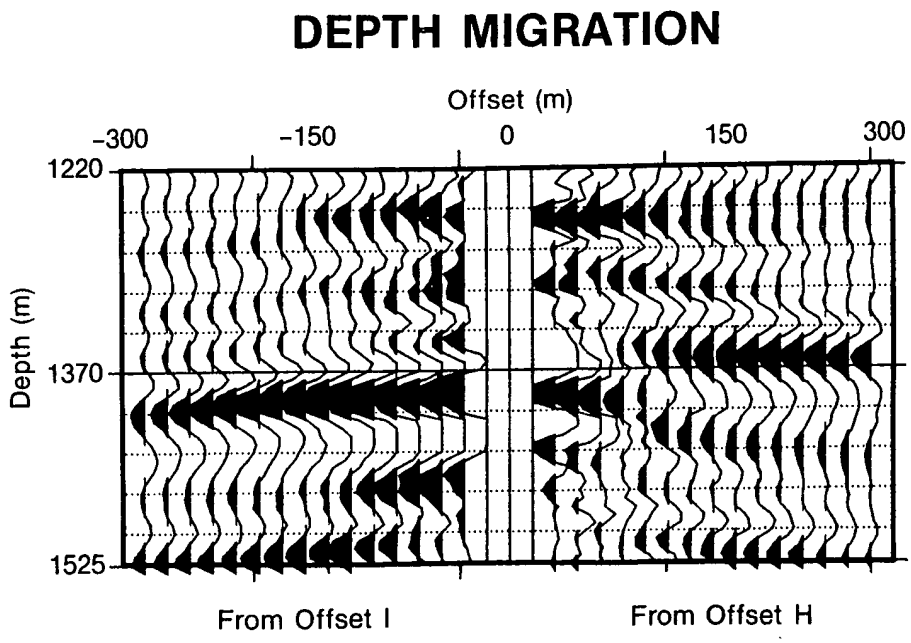

FIG. 7. Image created by migrating the *P*-to-*P* reflected wave field in the observed data shown in Figures 6. Notice the strong reflector just below 1370 m on the offset I image. This reflector continues across to the offset H image and then jumps up to just above 1370 m. This indicates the location of the reef on the offset H side of the well.

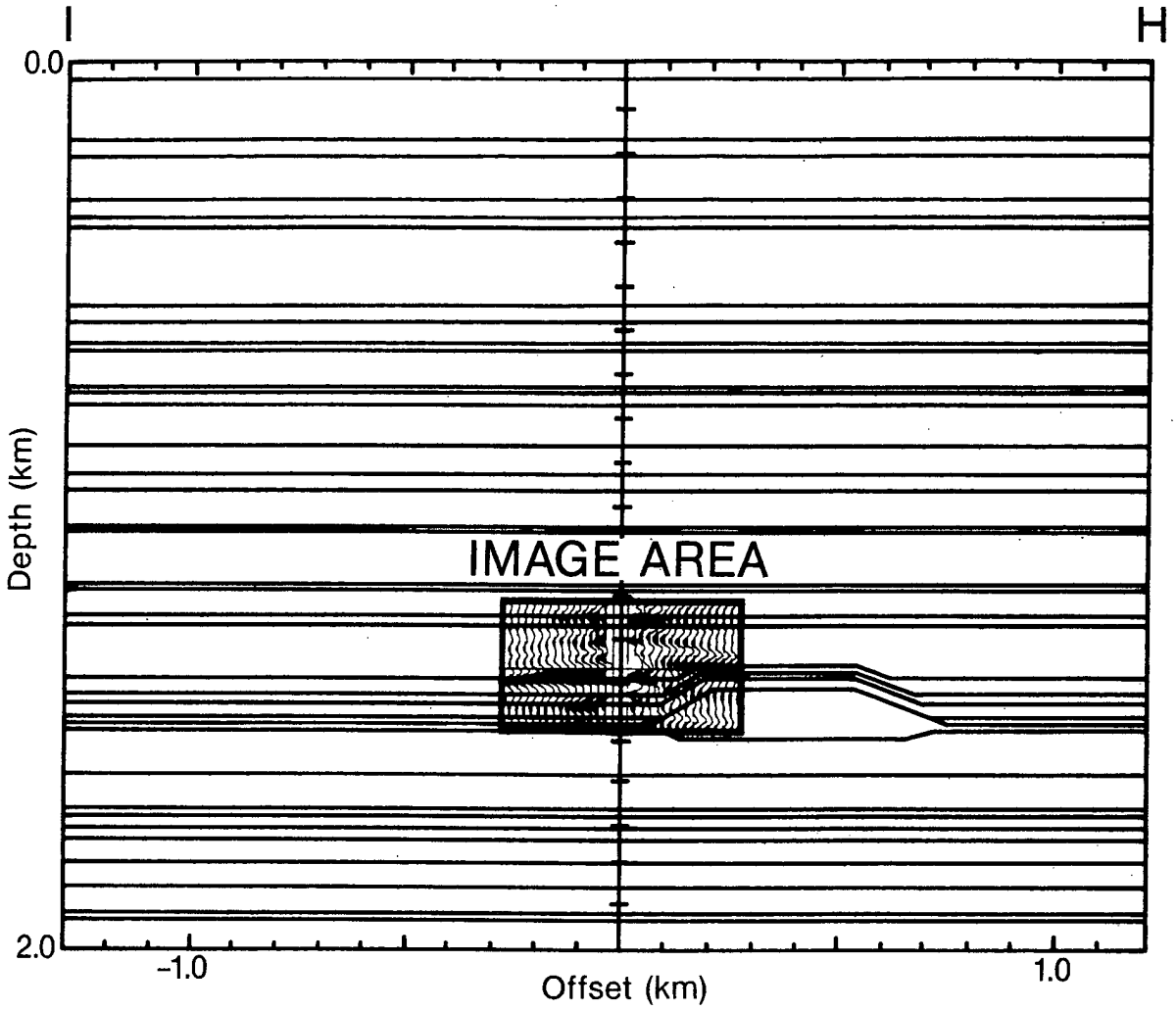

FIG. 8. Location of source offsets I and H with respect to the proposed location of the reef as determined from dip-meter analysis and VSP forward modeling. The migration image (Figure 7), shown superimposed on the model, indicates that the reef may be somewhat closer to the borehole than indicated by the proposed model.

such that only a few percent of the image points are missed by each ray fan. If an image point is missed by the ray fan from the source, then the source-to-image point traveltime will be zero. Similarly, a miss by a receiver ray fan causes the receiver-to-image point leg of the stacking time to be zero. With only a few misses, reflectors are still located accurately, but the image appears choppy—parts of the wavelets in the image are zero (e.g., see the left edge of the lowest reflector). This phenomenon is due to misses from the source. If the source-to-image point traveltime is zero, then none of the data from the receivers will be stacked at the correct time. Since the data in this example are synthetic, the traces are exactly zero except at the isolated times where the wavelet arrives. Thus, an incorrect stacking time which is too small due to a miss from the source will result in stacking the data at times for which the data are exactly zero. It is not serious if the receiver ray fans each miss a few percent of the image points, since each ray fan will miss different image points.

As a general rule, a denser fan of rays should always be shot from the source than from the receivers. Since the components of the stacking times from the source to the image points are computed only once, shooting a dense fan of rays from the source will substantially increase the accuracy of the stacking time with little additional computation cost. In practice, it is not uncommon to perform more than one migration with the migration velocity updated manually before each migration. In such cases, we suggest that sparse fans of rays should be shot from the receivers until the final migration. This will reduce the overall computation cost, since fewer rays will be shot.

Field data example

In this example PRKM is applied to VSP data collected in a borehole adjacent to a reef. These data were collected in Manistee County, Michigan by Compagnie Générale de Géophysique and the Earth Resources Laboratory of the Massachusetts Institute of Technology as part of an experimental group shoot for reservoir delineation. The objective of the experiment was to determine the location of a Niagaran

reef with VSP data, surface seismic data, and well-log data. We used a subset of the VSP data for this example. The VSP data were recorded in a well that was about 2000 m deep with 81 receivers separated from each other by approximately 9.14 m and a time sampling interval of 2 ms. Two source locations were occupied; H was offset 1220 m from the well on the on-reef side of the well and I was offset 1220 m on the off-reef side.

The *P*-wave velocity structure determined from well logs and 1-D waveform inversion, and the macromodel used for migration, are shown in Figure 5. The vertical component data for the two source locations I and H are shown in Figure 6. The data from each offset were migrated separately. The migrated images are shown juxtaposed in Figure 7. Migrating the data from one receiver took less than 60 s of CPU time on a VAX 11/750. In Figure 8, this image is reduced and shown overlain on the proposed model of the subsurface as determined from 3-D migration of surface seismic data, seismic modeling, and dip-meter analysis. The VSP migration image is consistent with the results obtained by the other methods and indicates that the reef may be somewhat closer to the borehole than indicated by the proposed model.

CONCLUSIONS

A rapid, variable velocity, prestack Kirchhoff migration is implemented by computing the Green's functions (traveltime and amplitude) with the paraxial ray method. Examples with synthetic and field data show that this technique produces high-quality images. This technique is computationally more efficient, by one order of magnitude, than traveltime and amplitude interpolation schemes. For traveltimes only, it is faster by less than one order of magnitude. Since the data can be migrated one receiver at a time, with currently available field computing systems migration of VSP data can be performed as the data are collected.

ACKNOWLEDGMENTS

We thank Roger Turpening and Carol Blackway for providing the velocity model for the Michigan reef site. This research was supported by the Reservoir Delineation-VSP Consortium at the M.I.T. Earth Resources Laboratory. We thank our colleagues Doug Foster, Brian Spies, and Nigel Wattrus for their helpful comments on our final draft of the manuscript.

REFERENCES

Berkhout, A. J., 1982, Seismic migration—Imaging of acoustic energy by wavefield extrapolation: A. Theoretical aspects: Elsevier Sci. Publ. Co.

Berryhill, J. R., 1979, Wave equation datuming: Geophysics, **44**, 1329–1344.

Ben-Menahem, A., and Beydoun, W. B., 1985, Range of validity of seismic ray and beam methods in general inhomogeneous media—I. General theory: Geophys. J. Roy. Astr. Soc., **82**, 207–234.

Beydoun, W. B., 1985a, Asymptotic wave methods in heterogeneous media: Ph.D. thesis, Mass. Inst. of Tech.

——— 1985b, Modeling with the paraxial ray method: 55th Internat. Mtg., Soc. Expl. Geophys., Expanded Abstracts, 473–475.

Beydoun, W. B., and Keho, T. H., 1986, The paraxial ray method: Fast computation of Green's functions for inverse scattering: Internat. Mtg., Soc. Expl. Geophys., Expanded Abtracts, 649–652.

——— 1987, The paraxial ray method: Geophysics, **52**, 1639–1653.

Beylkin, G., 1985, Imaging discontinuities in the inverse scattering problem by inversion of a causal generalized Radon transform: J. Math. Phys., **26**, 99–108.

Carter, J. A., and Frazer, L. N., 1984, Accommodating lateral velocity changes in Kirchhoff migration by means of Fermat's principle: Geophysics, **49**, 46–53.

Červený, V., Klimeš, L., and Pšenčik, I., 1984, Paraxial ray approximation in the computation of seismic wavefields in inhomogeneous media: Geophys. J. Roy. Astr. Soc., **79**, 89–104.

Červený, V., Popov, M. M., and Pšenčik, I., 1982, Computation of wavefields in inhomogeneous media—Gaussian beam approach: Geophys. J. Roy. Astr. Soc., **70**, 109–128.

Chang, W. F., and McMechan, G. A., 1986, Reverse-time migration of offset vertical seismic profiling data using the excitation-time imaging condition: Geophysics, **51**, 67–84.

Claerbout, J. F., 1970, Coarse grid calculations of waves in inhomogeneous media with application to delineation of complicated seismic structure: Geophysics, **35**, 407–418.

French, W., 1975, Computer migration of oblique seismic reflection profiles: Geophysics, **40**, 961–980.

——— 1974, Two-dimensional and three-dimensional migration of model-experiment reflection profiles: Geophysics, **39**, 265–277.

Gardner, G. H. F., French, W. S., and Matzuk, T., 1974, Elements of migration and velocity analysis: Geophysics, **39**, 811–825.

Gray, S. H., 1988, Computational inverse scattering in multi-dimensions: Inverse Problems, **4**, 87–101.

Hu, L., and McMechan, G. A., 1986, Migration of VSP data by ray equation extrapolation in 2-D variable velocity media: Geophys. Prosp., **34**, 704–734.

Keho, T. H., 1984, Kirchhoff migration for vertical seismic profiles: 54th Ann. Internat. Mtg., Soc. Expl. Geophys., Expanded Abstracts, 694–696.

Keho, T. H., and Wu, R. S., 1987, Elastic Kirchhoff migration for vertical seismic profiles: 57th Ann. Internat. Mtg., Soc. Expl. Geophys., Expanded Abstracts, 774–776.

Kuo, J. T., and Dai, T., 1984, Kirchhoff elastic migration for the case of noncoincident source and receiver: Geophysics, **49**, 1223–1238.

Levy, B. C., and Esmersoy, C., 1987, Variable background Born inversion by wavefield back-propagation: Submitted to SIAM J. Appl. Math.

Miller, D., Oristaglio, M., and Beylkin, G., 1984, A new formalism and an old heuristic for seismic migration: 54th Ann. Internat. Mtg., Soc. Expl. Geophys., Expanded Abstracts, 704–707.

Schneider, W., 1978, Integral formulation for migration in two and three dimensions: Geophysics, **43**, 49–76.

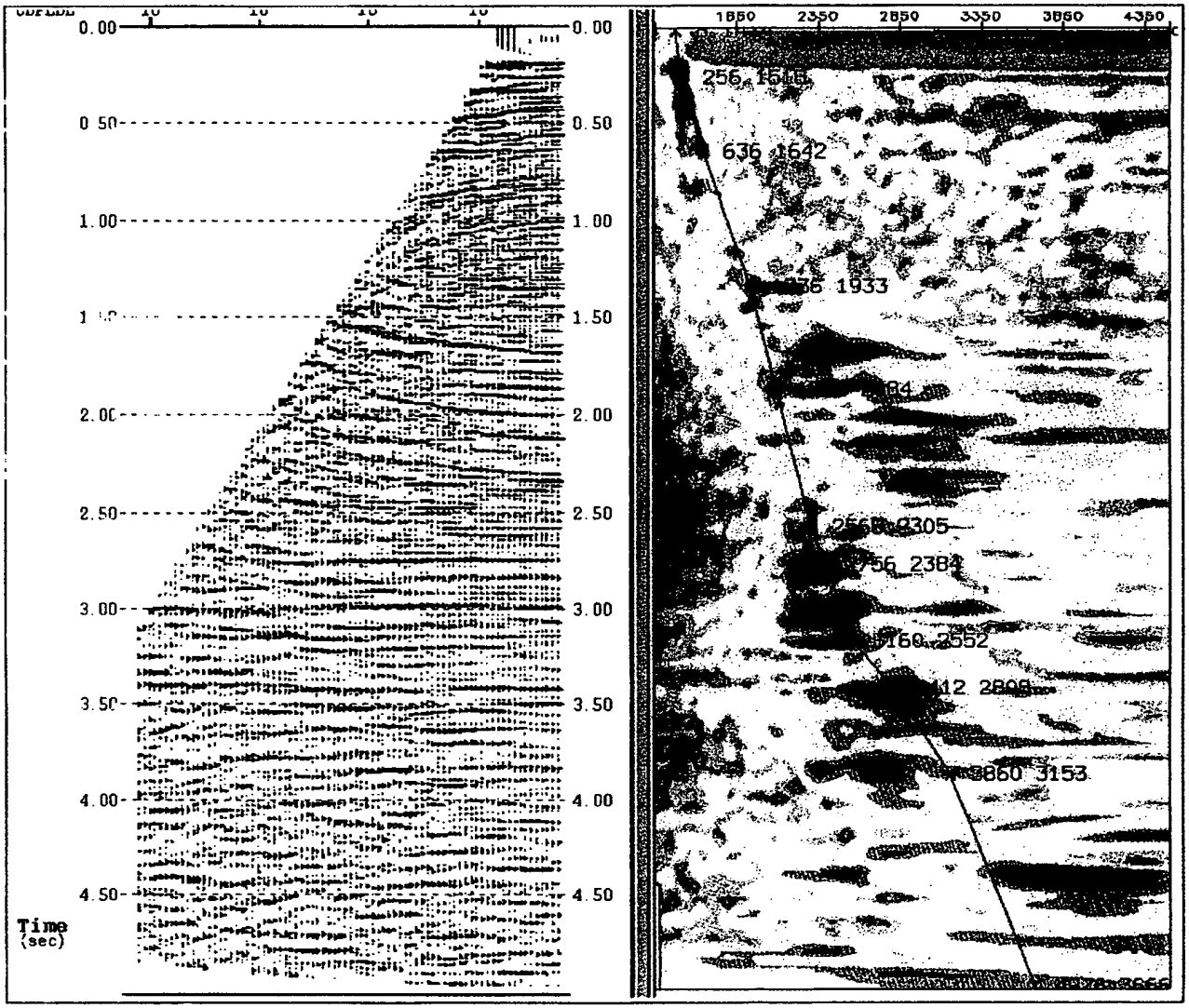

FIG. 5.3-21. CMP gather (left) and the velocity spectrum (right) as in Figure 5.3-20, with moveout correction applied to the data using the velocity function that is posted on the spectrum. This velocity function is appropriate for the nearly flat events associated with the sedimentary strata.

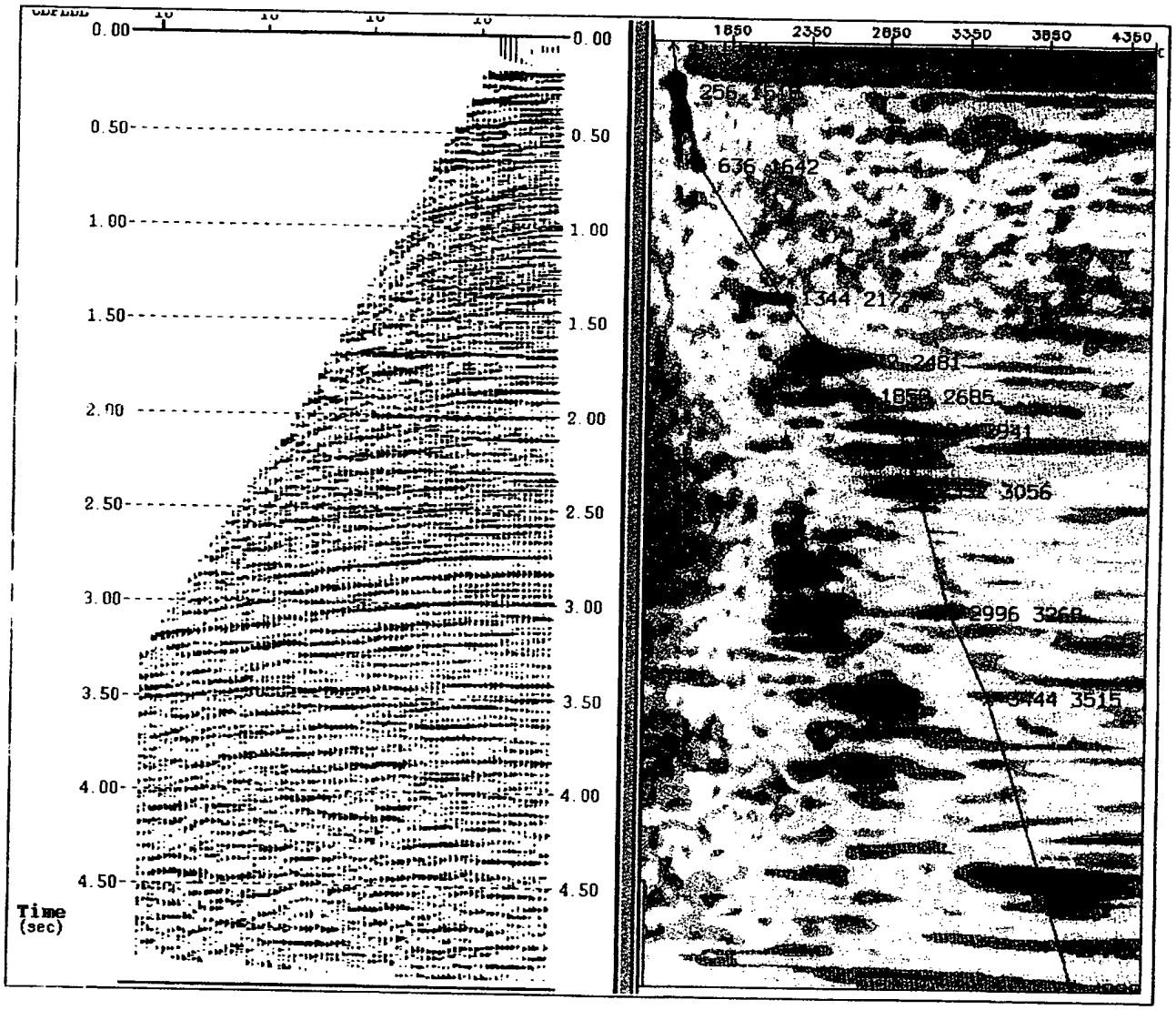

FIG. 5.3-22. CMP gather (left) and the velocity spectrum (right) as in Figure 5.3-20, with moveout correction applied to the data using the velocity function that is posted on the spectrum. This velocity function is appropriate for the steeply dipping events associated with the fault-plane reflections.

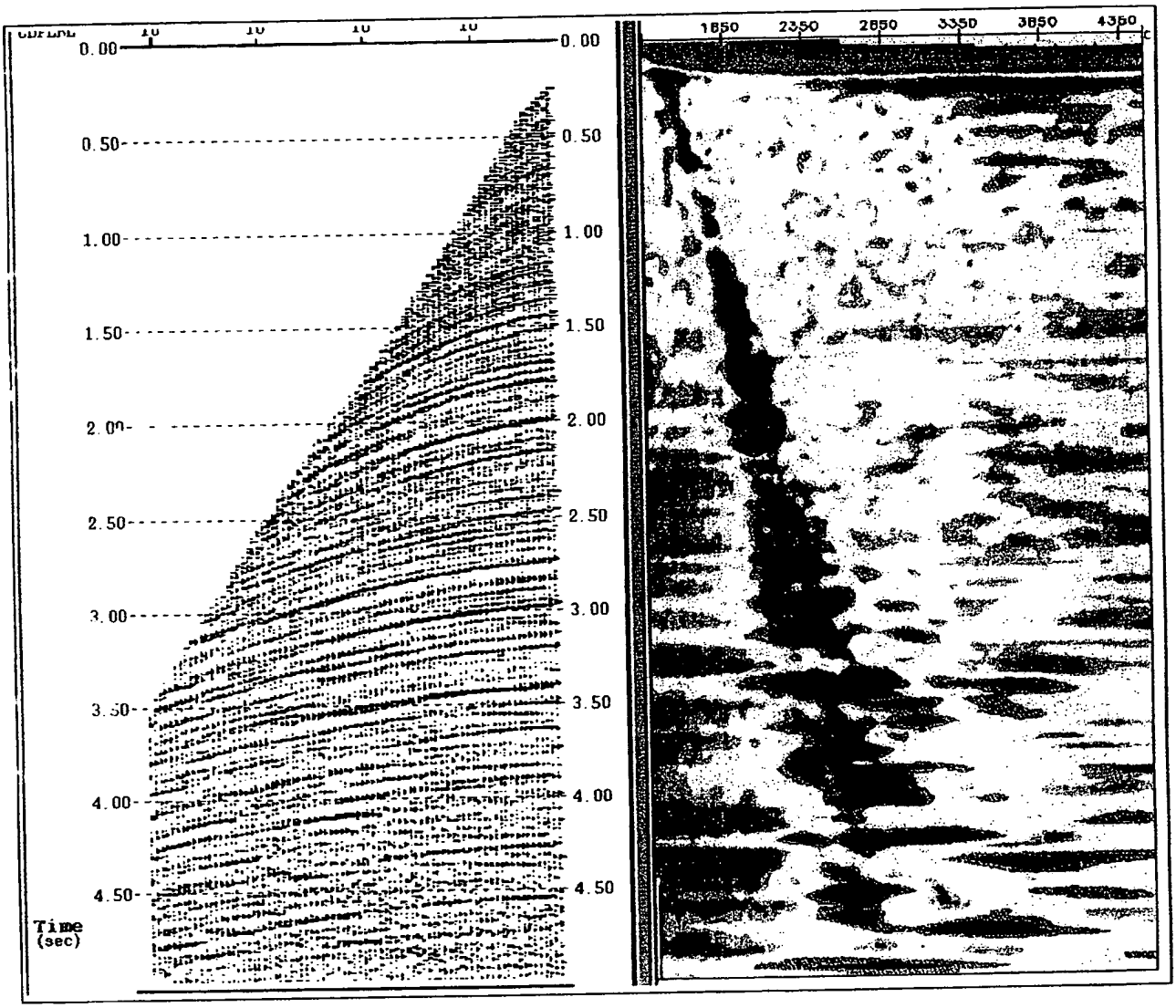

FIG. 5.3-23. CMP gather (left) and the velocity spectrum (right) at location A as in Figure 5.3-18 after DMO correction.

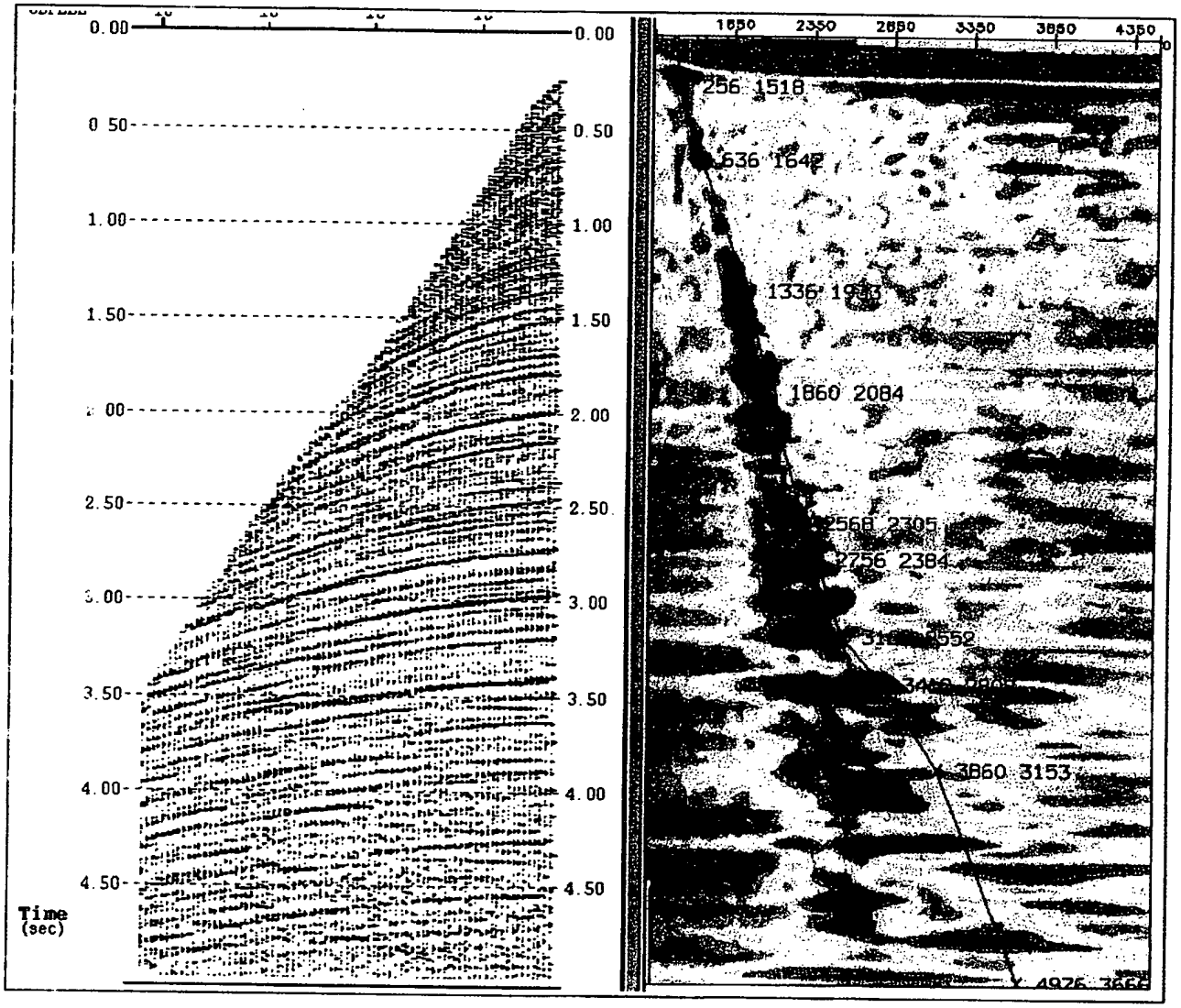

FIG. 5.3-24. CMP gather (left) and the velocity spectrum (right) as in Figure 5.3-23, with the velocity function of the gently flat events as in Figure 5.3-21 posted on the spectrum.

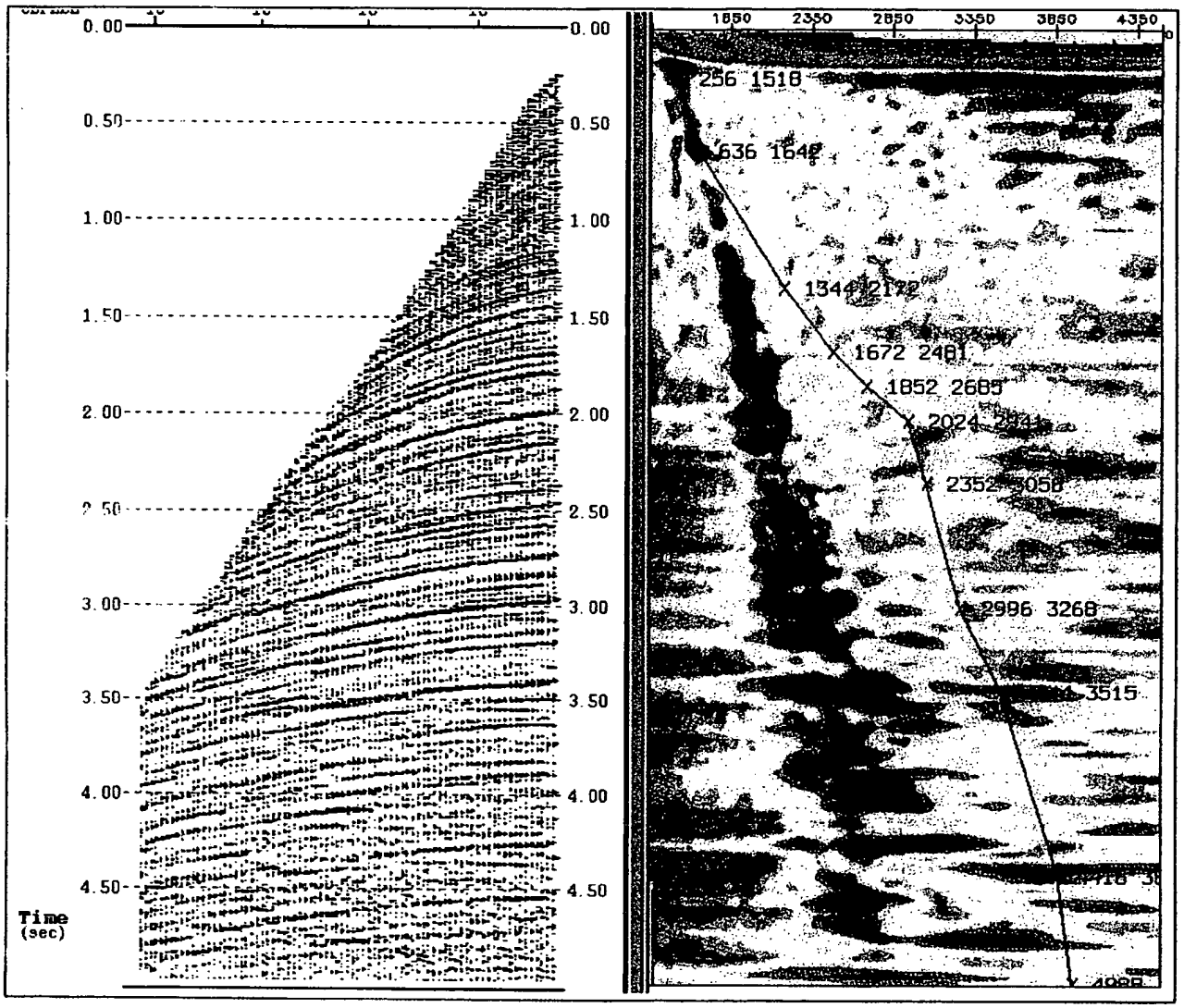

FIG. 5.3-25. CMP gather (left) and the velocity spectrum (right) as in Figure 5.3-23, with the velocity function of the steeply dipping events as in Figure 5.3-22 posted on the spectrum.

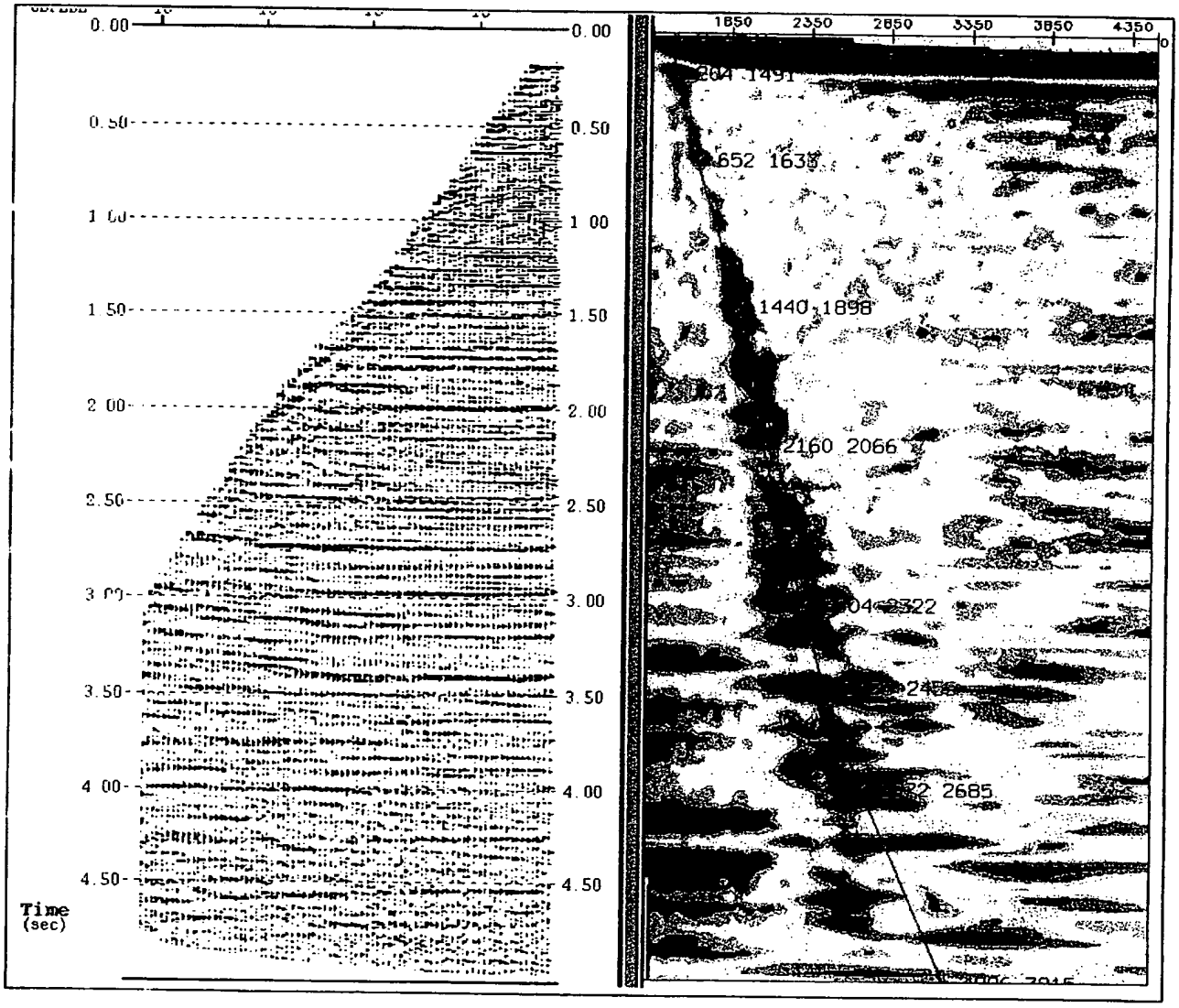

FIG. 5.3-26. CMP gather (left) and the velocity spectrum (right) as in Figure 5.3-23. with moveout correction applied to the data using the DMO-corrected velocity function that is posted on the spectrum.

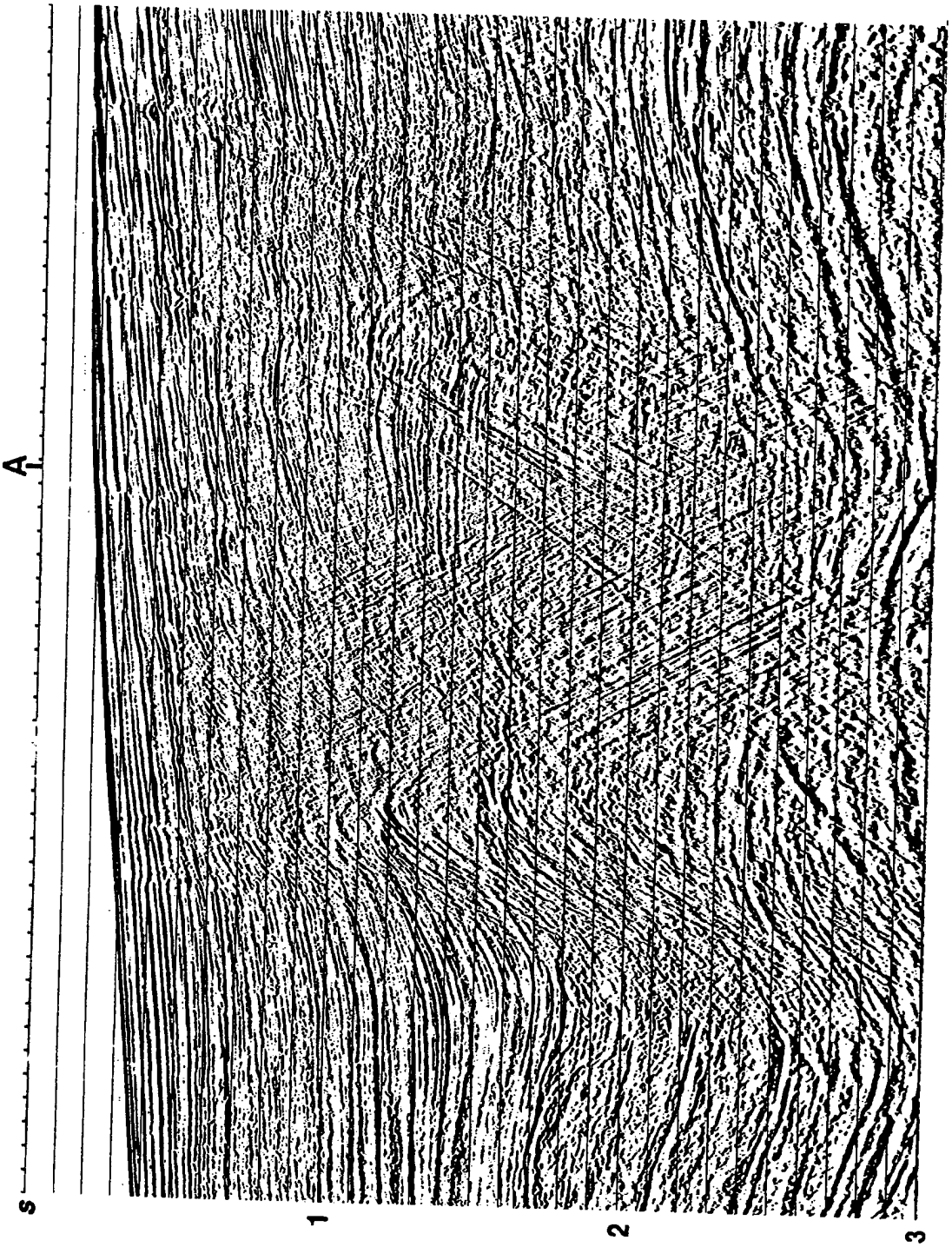

FIG. 5.3-27. A portion of a CMP stack with DMO correction. Velocity analysis at CMP location A is shown in Figure 5.3-23.

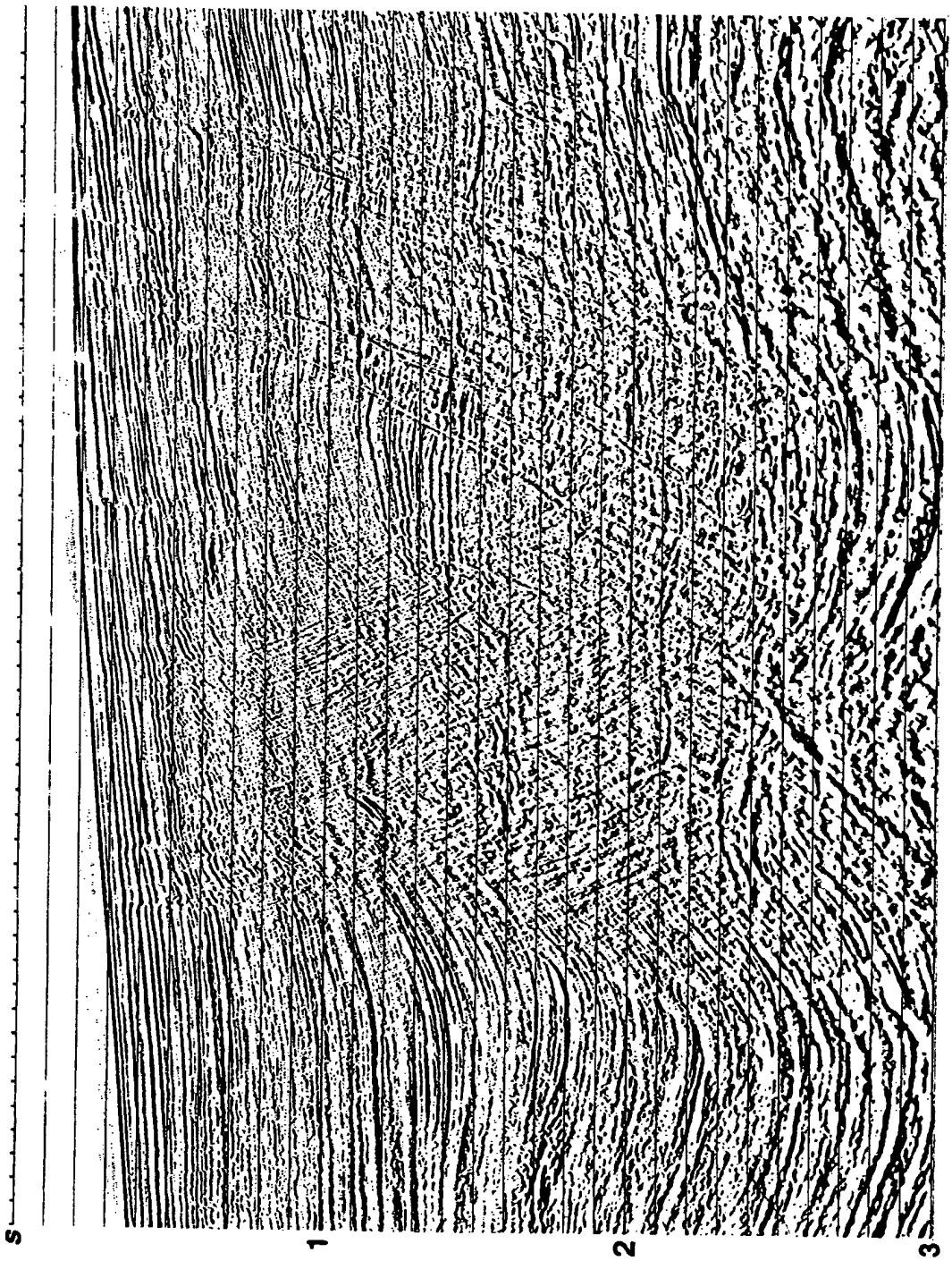

FIG. 5.3-28. Migration of the DMO stack shown in Figure 5.3-27.

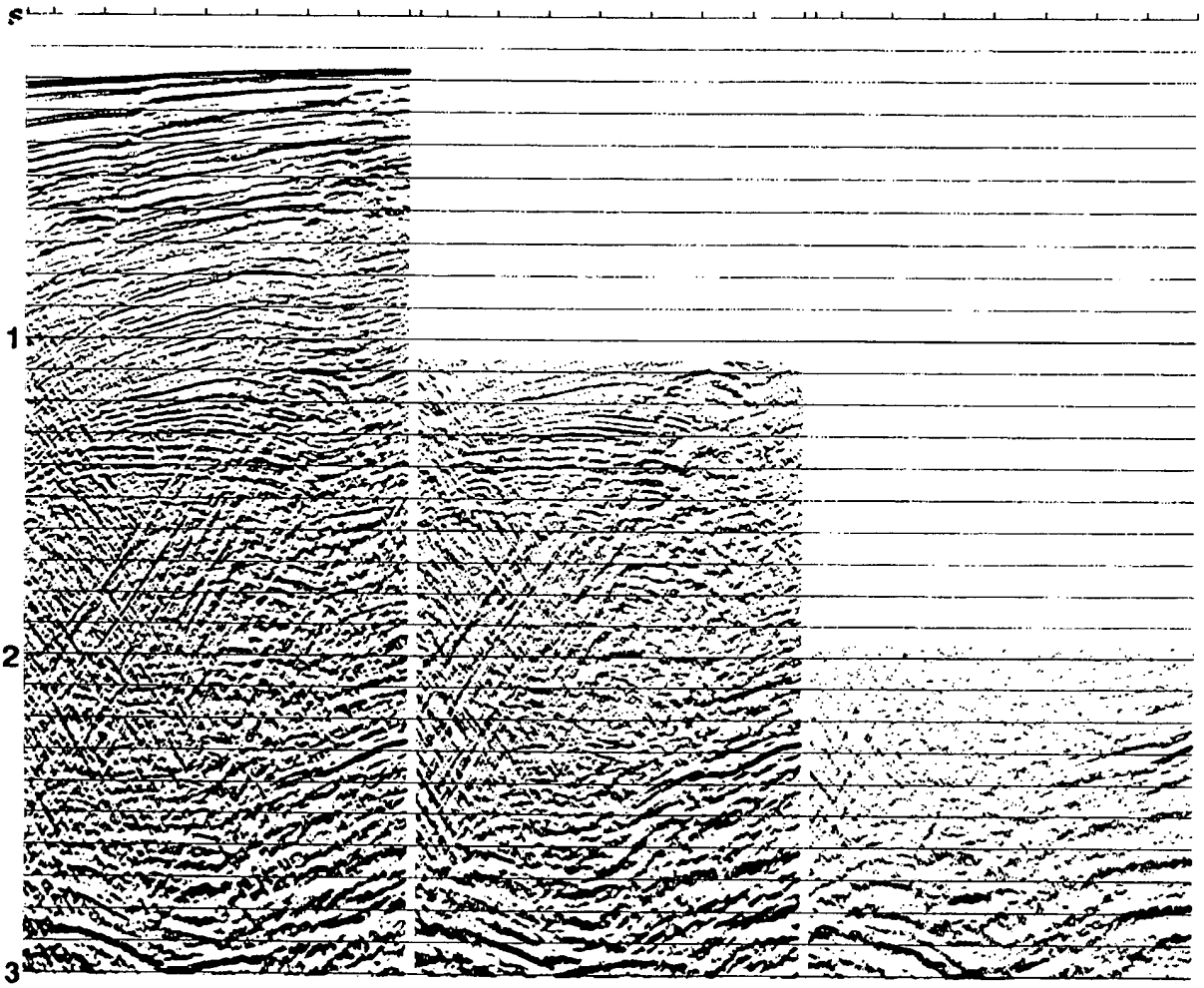

FIG. 5.3-29. Portions of three common-offset sections that coincide with the CVS panels shown in Figure 5.3-16 before DMO correction. Offsets are, from left to right, 500, 1500, and 2500 m.

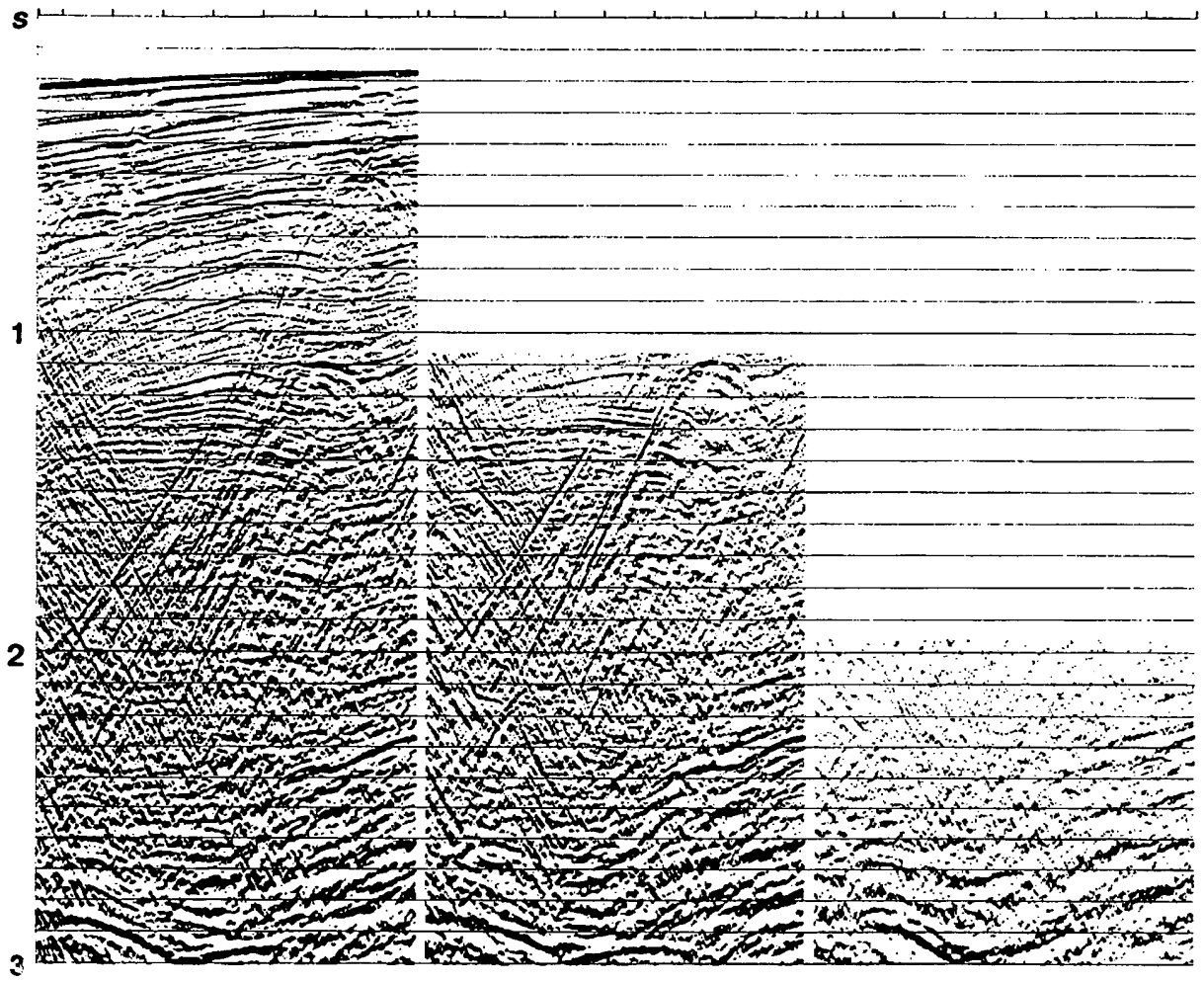

FIG. 5.3-30. Portions of three common-offset sections that coincide with the CVS panels shown in Figure 5.3-18 after DMO correction. Offsets are, from left to right, 500, 1500, and 2500 m.

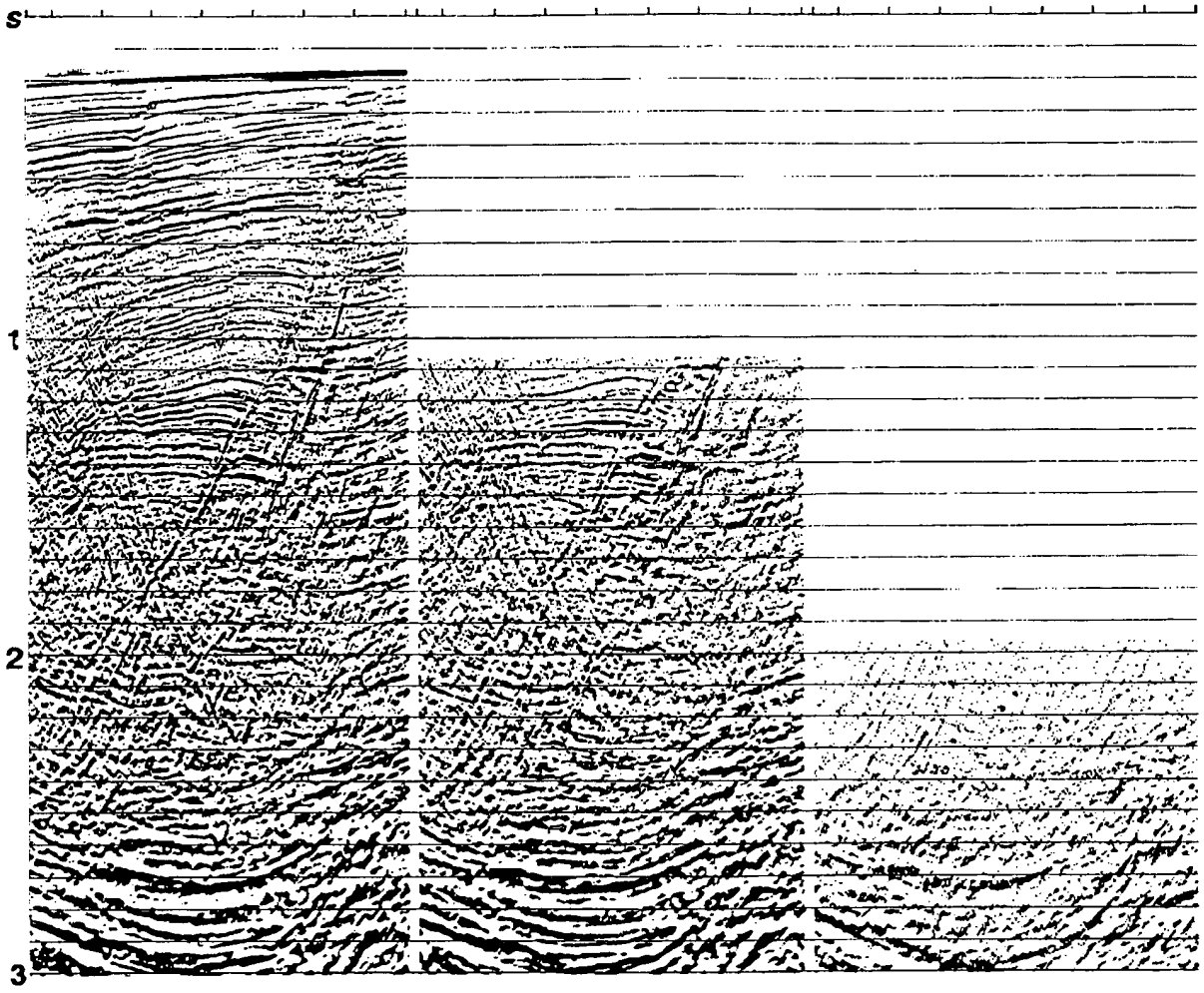

FIG. 5.3-31. Portions of three common-offset sections that coincide with the CVS panels shown in Figure 5.3-18 after DMO correction and common-offset migration. Offsets are, from left to right, 500, 1500, and 2500 m.

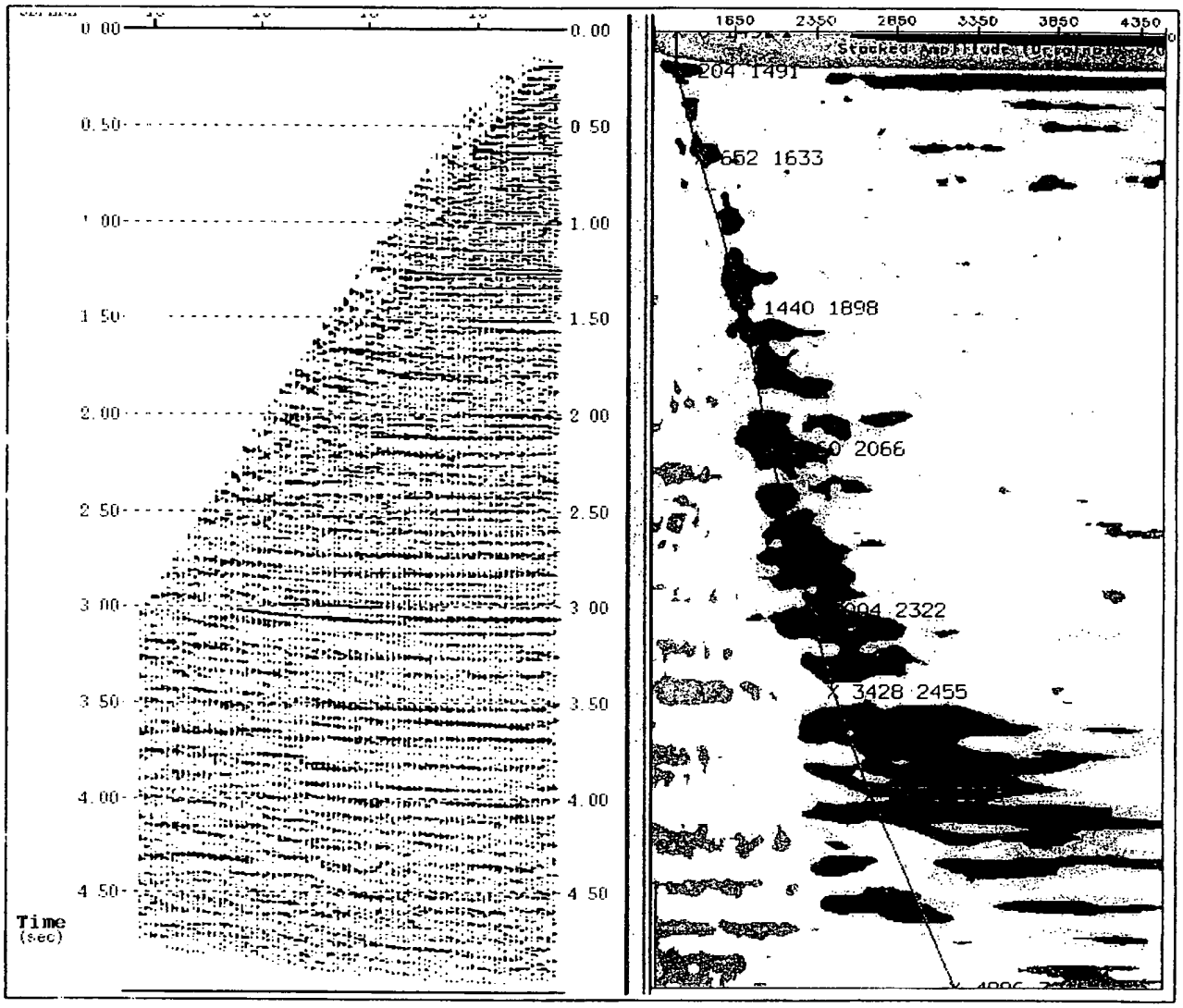

FIG. 5.3-32. CMP gather (left) and the velocity spectrum (right) at location A as in Figure 5.3-18, but after DMO correction and common-offset migration. The velocity function posted on the spectrum is the same as in Figure 5.3-26 derived from the data after DMO correction.

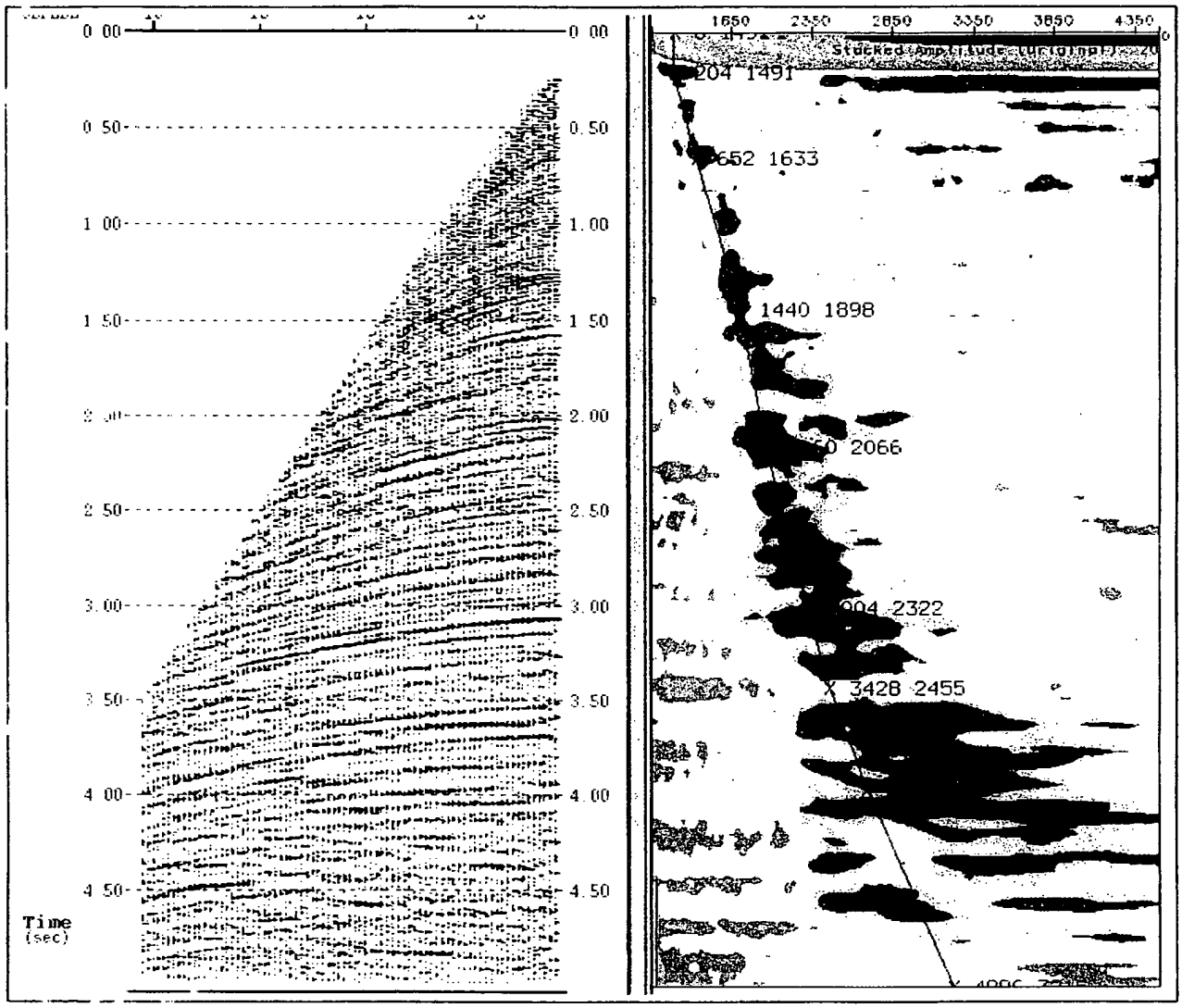

FIG. 5.3-33. CMP gather (left) and the velocity spectrum (right) as in Figure 5.3-32 after DMO correction, common-offset migration and inverse NMO correction using the velocity function posted on the spectrum. This velocity function is the same as in Figure 5.3-26 derived from the data after DMO correction.

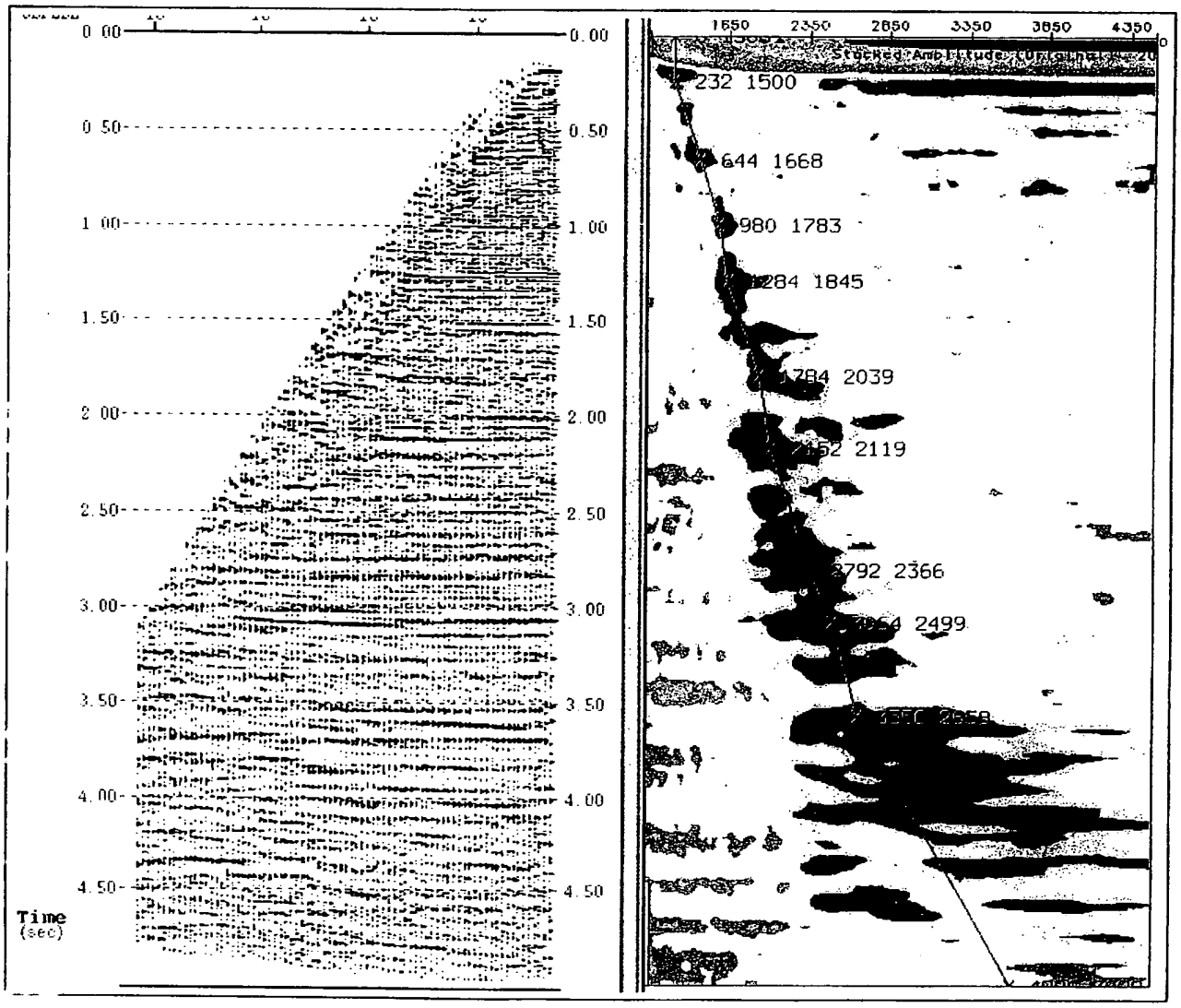

FIG. 5.3-34. CMP gather (left) and the velocity spectrum (right) as in Figure 5.3-33 after DMO correction, common-offset migration inverse NMO correction using the velocity function posted on the spectrum in Figure 5.3-33, and finally, NMO correction using the velocity function posted on the spectrum shown here and derived from the gather shown here after DMO correction and common-offset migration.

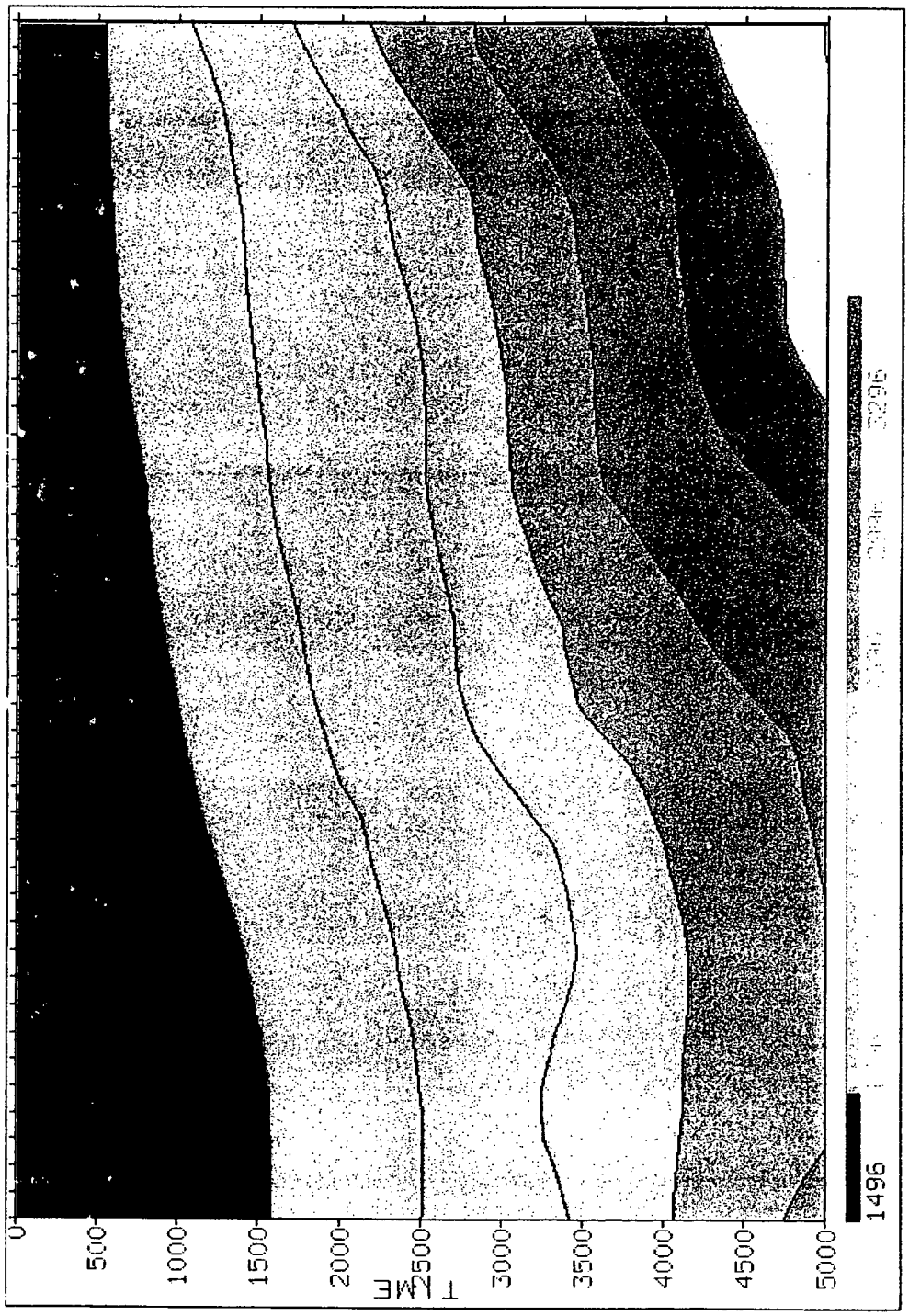

FIG. 5.3-35. Stacking velocity field derived from the velocity functions as in Figure 5.3-34 using data after DMO correction and common-offset migration. The resulting stacked section from prestack time migration is shown in Figure 5.3-36.

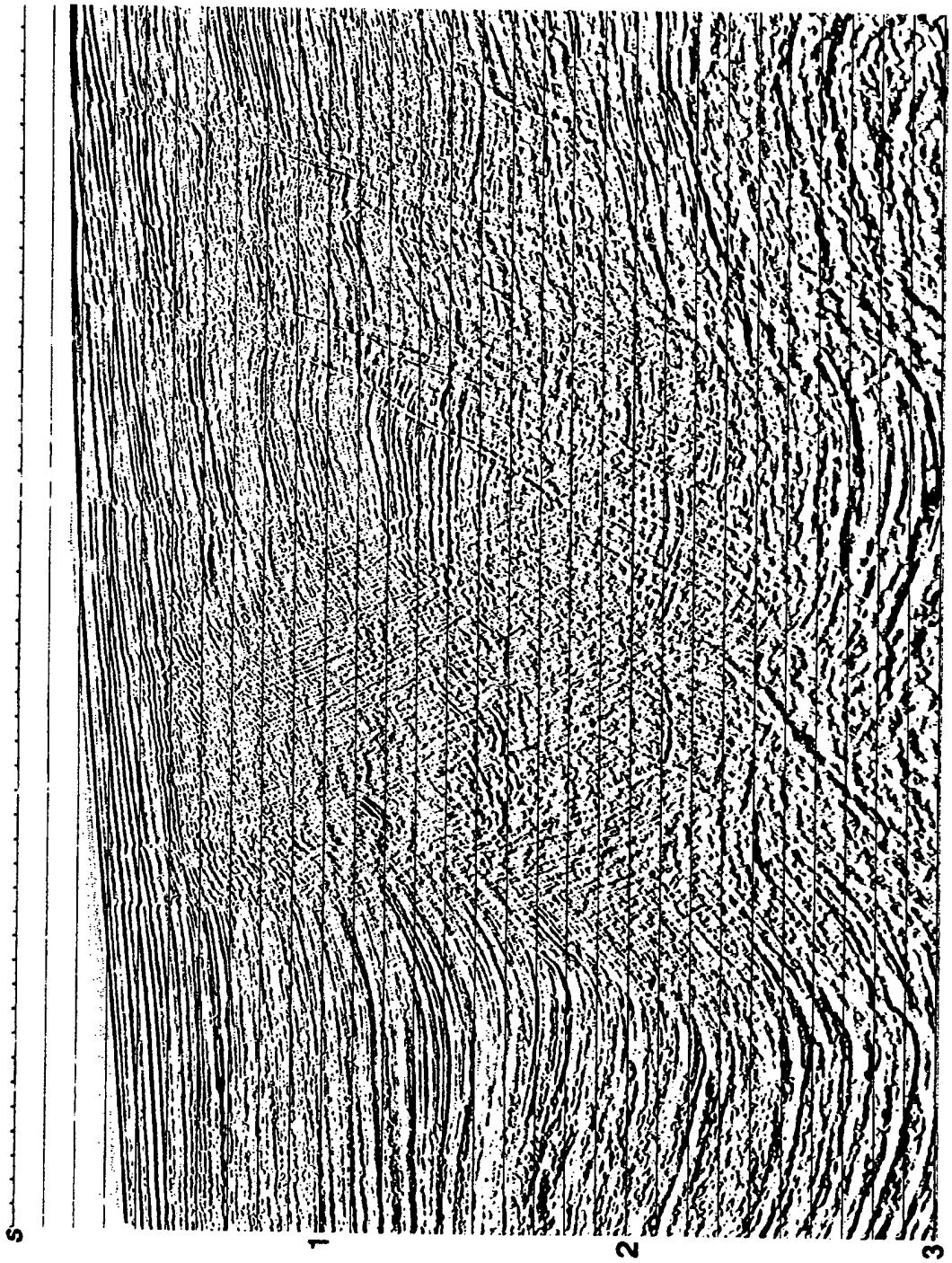

FIG. 5.3-36. The stacked section from prestack time migration based on the sequence that includes NMO and DMO corrections and common-offset migrations.

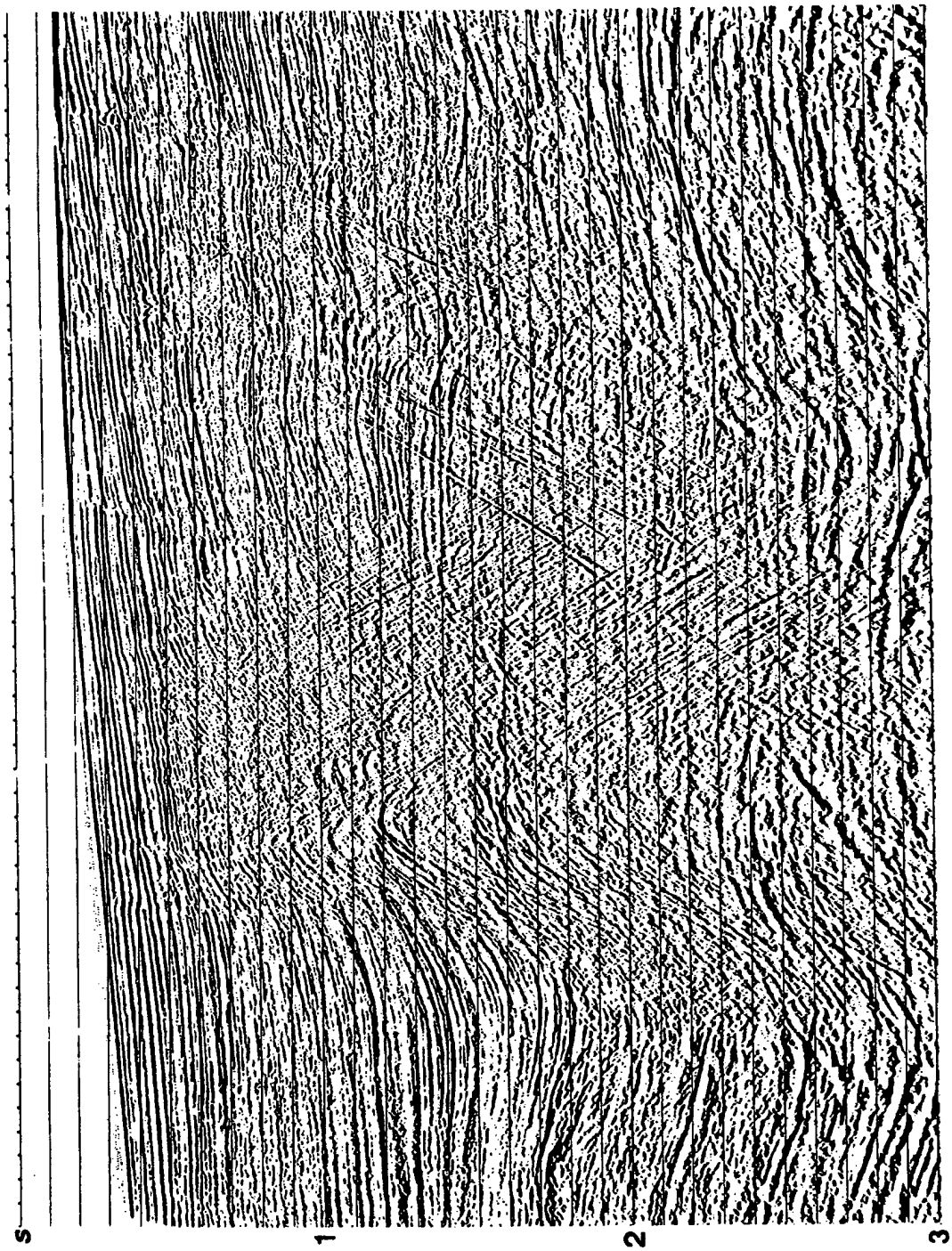

FIG. 5.3-37. Inverse migration of the stacked section in Figure 5.3-37.

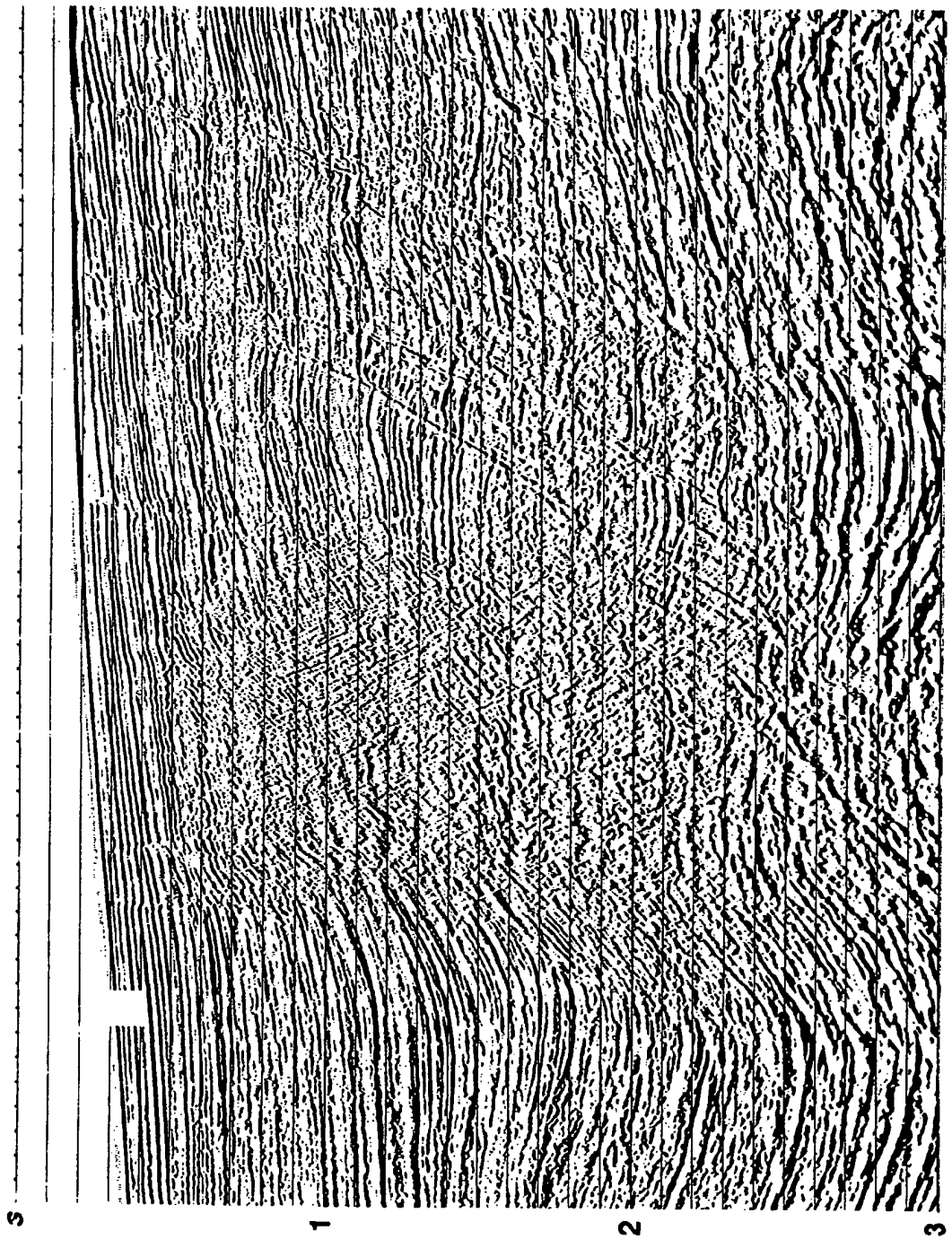

FIG. 5.3-38. Migration of the section in Figure 5.3-37 using the velocity field shown in Figure 5.3-35.

CMP gather using the low-velocity function in Figure 5.3-21, events that correspond to the gently dipping reflections are flattened whereas events that correspond to the steeply dipping reflections and diffractions are overcorrected. By applying NMO correction to the CMP gather using the high-velocity function in Figure 5.3-22, events that correspond to the steeply dipping reflections are flattened whereas events that correspond to the gently dipping reflections and diffractions are undercorrected.

The velocity spectrum at the same analysis location as for Figure 5.3-20 after the application of DMO correction shows a single, unambiguous velocity trend as shown in Figure 5.3-23. We have resolved the dip effect on stacking velocities and thus eliminated the multiple number of velocity picks as in Figure 5.3-20. As a result of the partial migration effect of DMO correction, energy is moved from one CMP location to another. Consequently, reflection-point smearing is removed and events on CMP gathers improvise a horizontally layered earth model.

For comparison, the low-velocity function associated with the gently dipping reflections in Figure 5.3-21 is superimposed on the velocity spectrum after DMO correction in Figure 5.3-24. As anticipated, the picks implied by the velocity spectrum after DMO correction are fairly close to the velocity function associated with the gently dipping reflections. Similarly, the high-velocity function associated with the steeply dipping reflections and diffractions in Figure 5.3-22 is superimposed on the velocity spectrum after DMO correction in Figure 5.3-25. In this case, the picks implied by the velocity spectrum after DMO correction are significantly lower than the velocity picks associated with the steeply dipping reflections.

The velocity analysis is repeated after DMO correction as shown in Figure 5.3-26. The picked velocities are then used to stack the data (Figure 5.3-27). Compare with the conventional CMP stack in Figure 5.3-14 and note that the DMO stack shown in Figure 5.3-27 has preserved the events with conflicting dips with different stacking velocities — the gently dipping reflections with the velocity function posted in Figure 5.3-21 and the steeply dipping fault-plane reflections with the velocity function posted in Figure 5.3-22. The resulting migrated section in Figure 5.3-28 shows a superior image of the fault blocks as compared to the migrated section without DMO correction (Figure 5.3-15).

For prestack time migration, we shall follow the same sequence as for the salt-flank data set.

(a) Sort the moveout-corrected CMP gathers to common-offset sections. Figure 5.3-29 shows portions of three selected common-offset sections. Note the presence of steeply dipping fault-plane reflections. Without DMO correction, CMP stacking fails to preserve these reflections as shown in Figure 5.3-14.

(b) Apply DMO correction to each common-offset section. Figure 5.3-30 shows portions of the three selected common-offset sections as in Figure 5.3-29 after DMO correction. Note the steeply dipping fault-plane reflections. With DMO correction, CMP stacking preserves these reflections as shown in Figure 5.3-27.

(c) Following DMO correction, each common-offset section is assumed to be a replica of a zero-offset section, and thus, can be migrated using a zero-offset migration algorithm. In this case, a single, vertically varying velocity function was used to migrate the NMO- and DMO-corrected common-offset sections. Figure 5.3-31 shows portions of the three selected common-offset sections as in Figure 5.3-30 after common-offset migration.

(d) Sort the migrated common-offset sections into CMP gathers. Events on these gathers are now assumingly close to correct subsurface positions after migration. Figure 5.3-32 shows a CMP gather after common-offset migration.

(e) Apply inverse NMO correction using the velocities picked before DMO correction and perform velocity analysis. The velocity spectrum computed from migrated data is shown in Figure 5.3-32 with the DMO velocities posted on it for comparison. The CMP gather after inverse NMO correction using the velocity function shown in Figure 5.3-32 is shown in Figure 5.3-33.

(f) Apply NMO correction using the velocity picks after migration (Figure 5.3-34). The velocity field derived from the post-migration velocity picks as in Figure 5.3-34 is shown in Figure 5.3-35, and the stack based on this velocity field is shown in Figure 5.3-36. This stack indeed is equivalent to prestack time-migrated section. Note that, however, common-offset migration actually was done using a single, vertically varying velocity function as in step (c).

(g) To obtain the migrated section with the velocity field (Figure 5.3-35) derived after common-offset migration, first perform inverse migration of the resulting stack from step (f) using the same velocity function as in step (c) to obtain a zero-offset section equivalent to an unmigrated stack as shown in Figure 5.3-37. Then, migrate this zero-offset section using the post-migration velocity field shown in Figure 5.3-35 to obtain the final result from prestack time migration sequence described here (Figure 5.3-38).

Common-Reflection-Point versus Common-Reflection-Surface Stacking

Conventional stacking is based on the notion of a common midpoint (CMP) and migration is based on the notion of a common reflection point (CRP). In both cases, we assume that reflections are represented by hyperbolas and reflectors are represented by points. Consider a seismic line from the Alberta Plains of Western Canada. The subsurface is just as flat as the surface over which you have recorded the data. When stacking the data, you can almost picture summing of the amplitudes in a CMP gather over all offsets along a hyperbolic trajectory associated with a zero-offset time and the resulting stacked amplitude being placed at a *point reflector* where the CMP raypaths converge conveniently. When migrating the stacked data, again, you sum the amplitudes along a hyperbolic trajectory and place the result at the apex of the hyperbola. You conveniently associate the apex of the latter hyperbola with a *point reflector* situated on the reflector. Whether it is a reflection hyperbola associated with a point reflector or a diffraction hyperbola associated with a point diffractor, the process of stacking and migrating the data involves summation of amplitudes along hyperbolas and placing the resulting sum to a point in the subsurface.

Now consider a seismic line from the Alberta Foothills where the cascaded flanks of the Rocky Mountains rise steeply. The subsurface is just as steep as the surface over which you have recorded the data. A diffractor still is a point whether it is in the Plains or in the Foothills, and you can still think of diffractions as hyperbolas so long as they are situated below a simple overburden. Fortunately, you can also think of reflections as hyperbolas. No longer, however, can you associate a reflection hyperbola on your CMP gather with a single point reflector; instead, you have reflection points dispersed along the reflector (Section E.1). This is when you have to introduce DMO correction to account for the reflection-point dispersal (Section 5.1). Once the reflection-point dispersal is removed, the resulting stack can be considered equivalent to a zero-offset section which you can migrate, again, using the hyperbolic summation rule. Thus you have been able to overcome the Foothills problem of steeply dipping events.

Finally, consider a seismic line from the Canadian Thrust Belt west of the Foothills. The subsurface is just as complex as it appears on the surface over which you have recorded the data. A diffractor situated below the complex overburden structure caused by the overthrust tectonics stays as a point; no longer, however, can you associate it with a hyperbolic traveltime. Instead, when migrating the data, you have to deal with a complex, distorted traveltime trajectory. And neither can you associate the reflections with hyperbolic traveltimes. Instead, when stacking the data, you have to deal with a nonhyperbolic moveout trajectory associated with many reflection points scattered around in the subsurface (de Bazelaire, 1988).

So the simple hyperbolic and point rules of the Plains or the Foothills are no longer applicable in the Thrust Belt. To overcome the first problem -- migration of data in the presence of strong lateral velocity variations associated with complex overburden structures in the Thrust Belt, you may decide to do the imaging in depth (Section 8.0) instead of imaging in time (Section 4.0). Earth imaging in depth requires earth modeling in depth (Section 9.0) -- a challenge much higher than the imaging itself. To overcome the second problem -- stacking of data with nonhyperbolic moveout, you may combine it with the first problem and pursue a rigorous solution by doing the imaging not just in depth but also before stack.

Note that, insofar as stacking and imaging in time or in depth, we choose to map events to common-reflection points. By way of DMO correction, we map events to common-reflection points in their *unmigrated positions*. Similarly, by way of prestack time migration, we map events to common-reflection points in their *migrated positions*. De Bazelaire (1988) and Gelchinsky (1988) pointed out that, rather than associating the recorded data with *common-reflection points*, we should associate the recorded data with *common-reflection surfaces*. As such, when stacking the data, rather than constricting the summation of amplitudes to within a single CMP gather, data may be focused to a common-reflection surface (CRS) using multiple shots and receivers (Gelchinsky, 1988; and Höcht, 1998).

The theory and practice of the CRS stacking method (Gelchinsky, 1988; Tygel et al., 1997; Gelchinsky et al., 1999a,b; Höcht, 1998; Berkovitch et al., 1998; Landa et al., 1999) suggest that it is indeed related to prestack time migration when the medium velocities are judged to be within the acceptable bounds for the latter. The CRP gathers from prestack time migration and the CRS gathers both are created by including in the summation aperture multiple numbers of CMP gathers. The difference is that the CRP gathers are associated with events in their *migrated positions*, whereas the CRS gathers are associated with events in their *unmigrated positions*. So, migration of the CRS stack should resemble the section from prestack time migration.

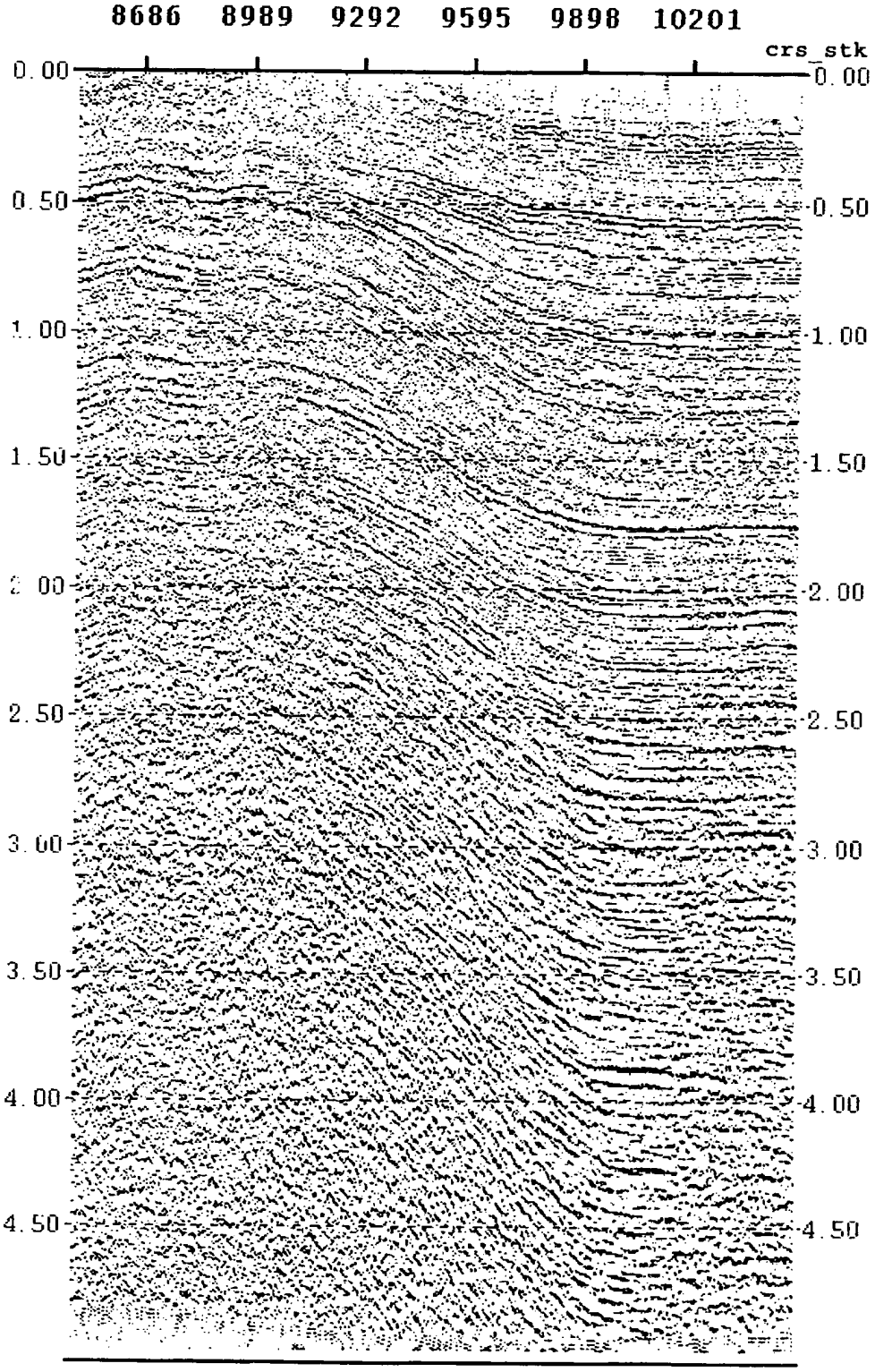

FIG. 5.3-39. A common-reflection-surface (CRS) stack. (Data courtesy Saudi Aramco.)

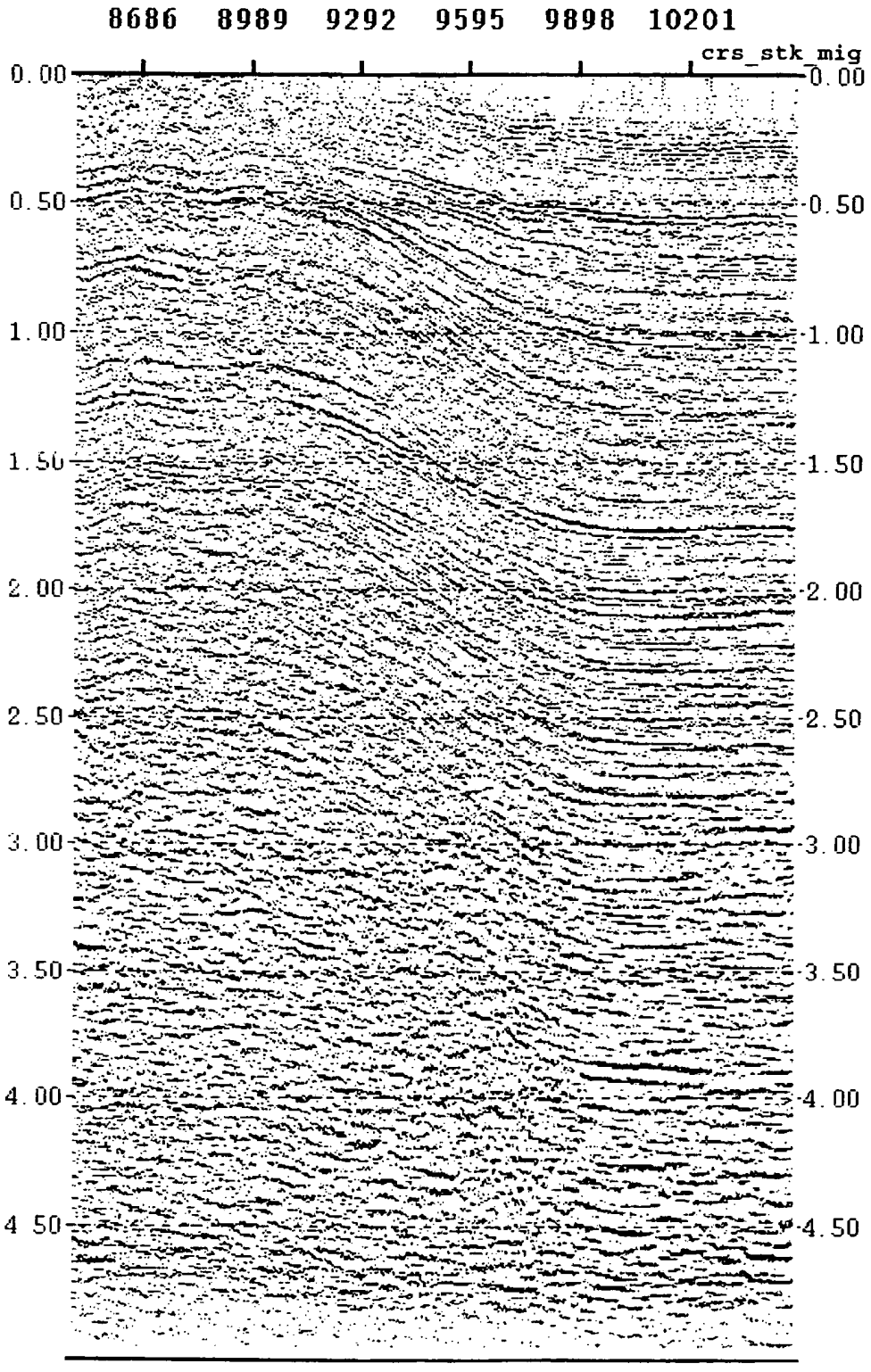

FIG. 5.3-40. Migration of the common-reflection-surface (CRS) stack shown in Figure 5.3-39.

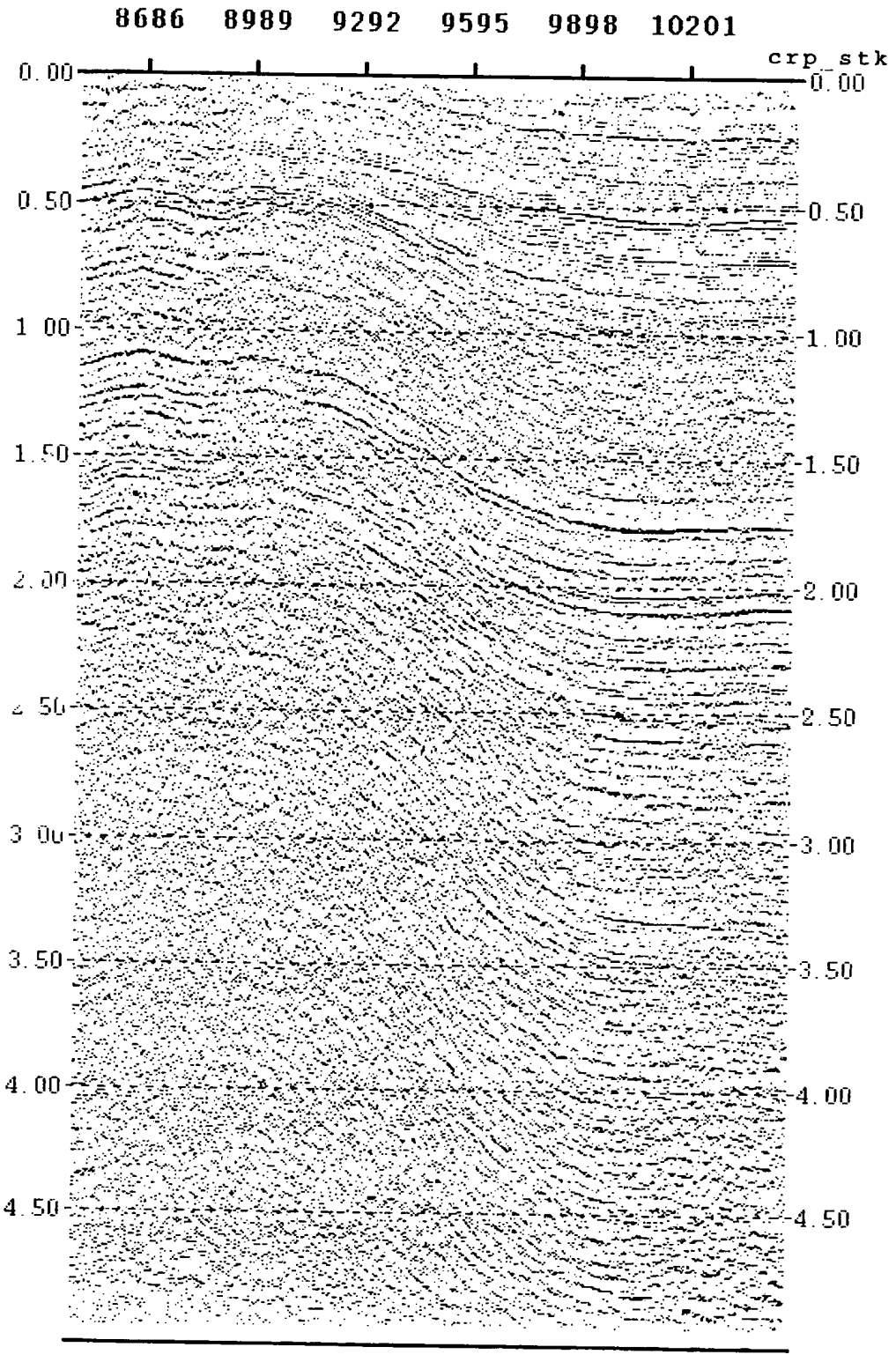

FIG. 5.3-41. A common-reflection-point (CRP) stack of the data as in Figure 5.3-40 derived from prestack time migration.

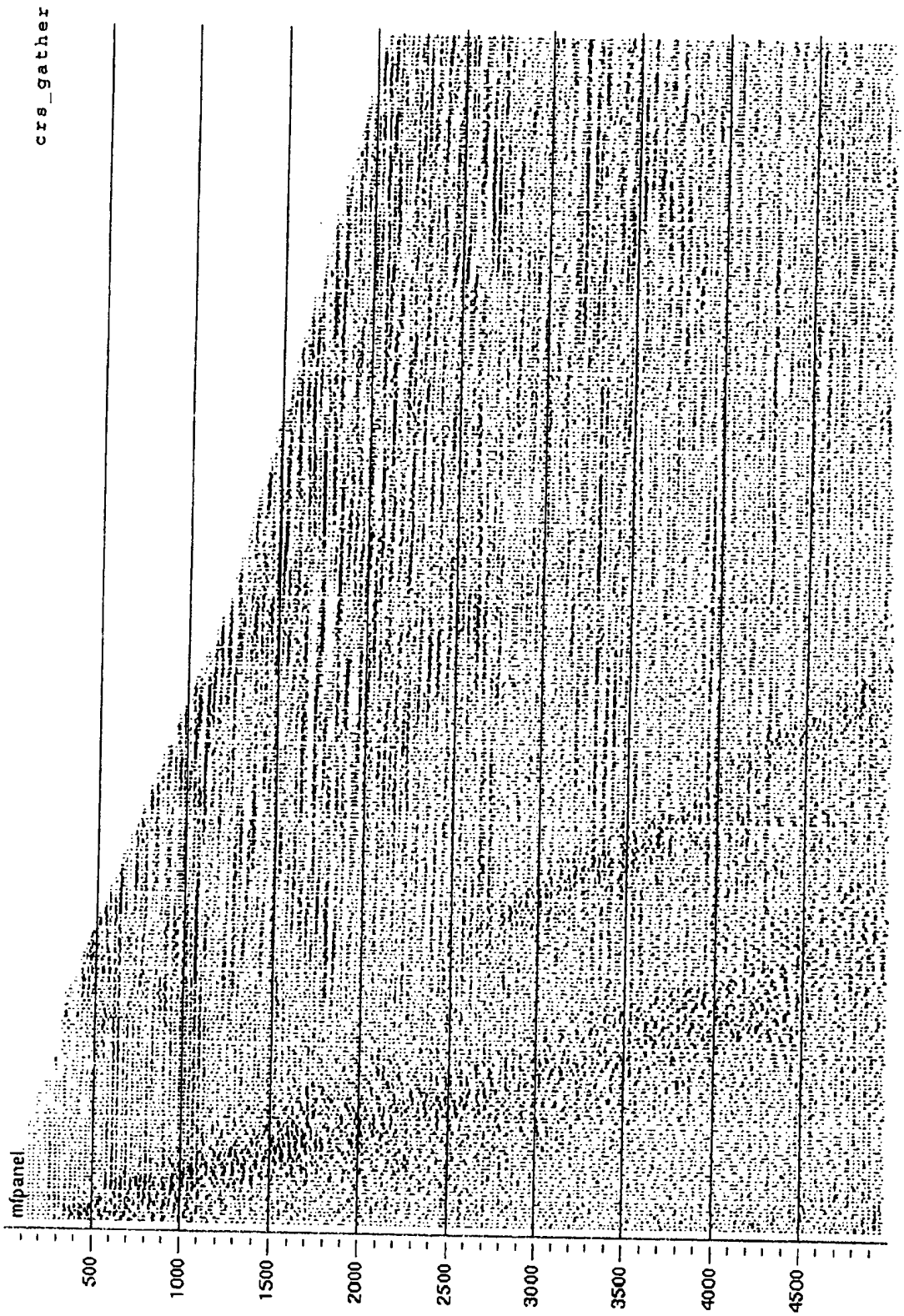

FIG. 5.3-42. A common-reflection-surface (CRS) gather associated with the CRS stack shown in Figure 5.3-39.

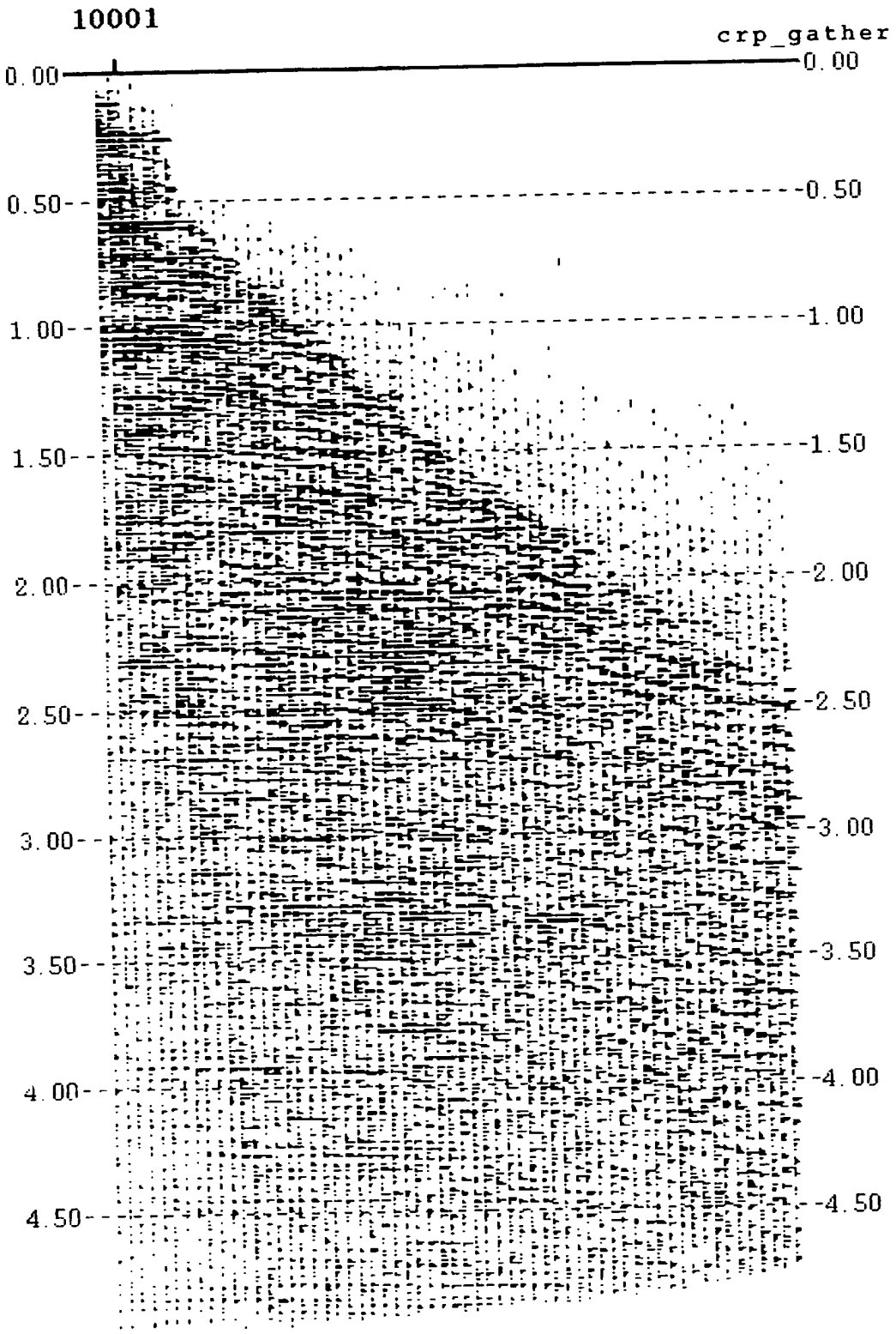

FIG. 5.3-43. A common-reflection-point (CRP) gather associated with the CRP stack shown in Figure 5.3-41.

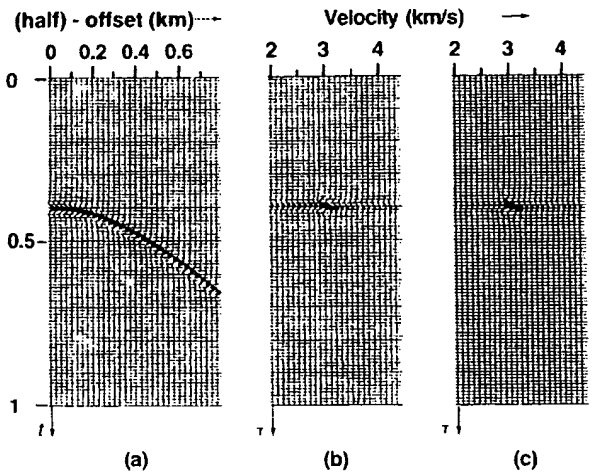

FIG. 5.4-1. (a) A CMP gather containing a single reflector in a constant-velocity medium; (b) velocity spectrum derived by migrating the CMP gather using a number of constant velocities and displaying the zero-offset trace from each migration; (c) velocity spectrum derived by NMO correcting and stacking the CMP gather using the same range of constant velocities as in (b). Each trace in (b) is a zero-offset trace, while each trace in (c) is a CMP stacked trace.

Figure 5.3-39 shows a CRS stack from an area with low-relief structures. The field data were recorded with 240-fold coverage. For CRS processing, the negative offsets were discarded and the near one-half of the positive offsets were kept; thus the reduced data used to create the CRS stack had 60-fold coverage. For prestack time migration, the original 240-fold data were first reduced to 60-fold by partial stacking. The migrated CRS stack shown in Figure 5.3-40 is comparable to the CRP stack derived from prestack time migration shown in Figure 5.3-41. In the present example, five CMP gathers were used to create one CRS gather with 300 traces as shown in Figure 5.3-42. The 60-fold CRP gather at the same location as for the CRS gather of Figure 5.3-42 is shown in Figure 5.3-43.

Practical refinements to various approaches to CRS stacking and imaging, including extensions to 3-D, are under current investigation. As to what extent the technique will be applied routinely to seismic data remains to be seen.

5.4 MIGRATION VELOCITY ANALYSIS

Velocity estimation, CMP stacking, and migration generally are considered independent processes. However, they all have a common theoretical base — the scalar wave equation. Solution of this equation allows downward extrapolation of a seismic wavefield recorded at

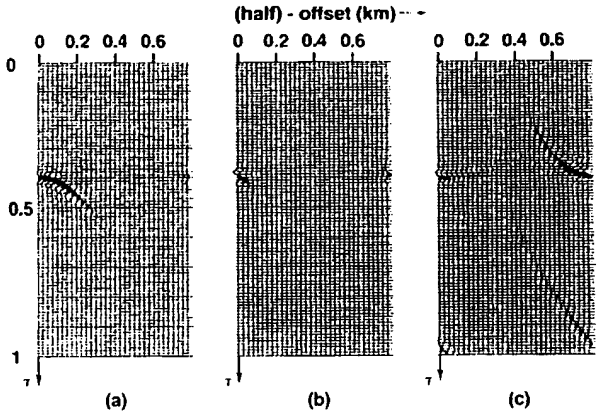

FIG. 5.4-2. Migrations of the CMP gather in Figure 5.4-1a using velocities that are (a) lower than the medium, (b) the same as the medium, and (c) higher than the medium velocity. (Note the wraparound effect in (c) that is inherent to the phase-shift method used in this analysis.)

the earth's surface. In turn, downward extrapolation provides a basis for CMP stacking and migration (Clayton, 1978; Yilmaz and Claerbout, 1980). Because the processes of CMP stacking and migration require velocity information, they also can be used to obtain a velocity estimate (Taner and Koehler, 1969; Gardner et al., 1974).

For example, consider the problem of conventional velocity estimation for stacking. Figure 5.4-1a shows a CMP gather over a single horizontal reflector. Select a constant velocity, apply NMO correction, and stack the traces in the gather. Next, place this stack trace onto the plane of velocity versus two-way zero-offset vertical time (v, τ) as shown in Figure 5.4-1c. By stacking the gather with different constant velocity values, the entire (v, τ) plane is filled with stacked amplitudes. (In this section, the variable τ is used specifically to define the vertical two-way zero-offset time, $\tau = 2z/v$.)

We now consider the migration process. For a horizontally stratified earth, as in Figure 5.4-1a, we cannot distinguish between a CMP gather and a common-shot gather (CSG). Moreover, since a CSG is a true wavefield created by a single shot and recorded by many receivers, it seems reasonable that the CMP gather in Figure 5.4-1a can be migrated by treating the reflection hyperbola as if it were a diffraction hyperbola. Assuming there is no velocity information, we migrate with various trial constant velocities and evaluate the results. Figure 5.4-2 shows three different attempts at migrating the CMP gather of Figure 5.4-1a. In one attempt (Figure 5.4-2a), too low a velocity was used; hence, the event was undermigrated. In another attempt, too high a velocity was used and the event was overmigrated (Figure

(3)

Anti-aliased Kirchhoff 3-D migration

David E. Lumley*, Jon F. Claerbout, and Dimitri Bevc, *Stanford University* ★ SM4.6

SUMMARY

A significant degradation in the quality of Kirchhoff migration images can arise when the migration operator summation trajectory is too steep for a given input seismic trace spacing and frequency content. This phenomenon is called "operator aliasing" and is strictly distinct from and independent of data aliasing. Unfortunately, the conditions which lead to significant operator aliasing are common in most 3-D Kirchhoff migration work, due to the sparse and irregular nature of 3-D acquisition geometries, and the need to minimize the size of 3-D migration input data volumes.

We anti-alias the migration operators "on the fly" with N-point triangle filters. Using a Z-transform representation, we reduce each N-point triangle filter operation to an efficient three-point filter operation, with the added minor overhead of a causal and anticausal integration of the input trace data prior to migration. Our anti-aliased migration is computationally efficient since it requires about the same number of floating point operations as a conventional Kirchhoff migration, and is conservative in its memory use since it does not require storage of multiple trace-data copies to implement the anti-aliasing. Our anti-aliased migration is accurate in that it applies local anti-alias filters separately for each of the many migration operators which pass through a given input data point.

We demonstrate our method with a 3-D implementation on a massively parallel Connection Machine CM-5, and compare our new anti-aliased Kirchhoff migration to a conventional aperture-weighted Kirchhoff migration in an application to a 3-D marine seismic data example. Our results indicate that our anti-aliasing method greatly enhances the 3-D resolution of steep salt-sediment interfaces and faults, and suppresses false reflections caused by conventional Kirchhoff-migration aliasing artifacts. Our method is applicable to other space-time Kirchhoff operations such as NMO velocity-stacking and DMO.

INTRODUCTION

The process of seismic migration involves a mapping of the input seismic trace data by a migration operator to the output structural image. Spatial aliasing of the migration process can be problematic in all three domains: data, operator and image. These three types of spatial aliasing are distinct and independent, although they are often confused.

Aliasing defined

Data aliasing occurs when there are seismic frequencies f and dips θ along reflection and diffraction events in recorded seismic data which violate the following criterion: $f \leq f_d = v_r/(4 \sin\theta_r \Delta x)$. The term f_d is the maximum unaliased frequency in the data for a given trace spacing Δx, a velocity v_r at the receiver location, and a local plane-wave incident angle θ_r at the recording surface. Once data have been aliased during the recording process, it is difficult to suppress subsequent processing artifacts except to reshoot the survey at a finer group spacing, or try to interpolate the original data without interpolating the aliases, e.g., Spitz (1991) and Claerbout (1992). Yilmaz (1988) gives a good overview of data aliasing and its effects on all methods of migration.

Image aliasing occurs when the output sampling of the image space is too coarse to properly represent migrated dips. This is mostly a cosmetic problem and can be remedied by choosing an appropriate image mesh upon which to estimate the migrated structural image. Note that the Kirchhoff-migrated values at each mesh point in an aliased image space are uncontaminated and correct (assuming no data or operator aliasing). For example, a single migrated output trace at a well location may be entirely accurate without having to estimate any adjacent migrated traces. This "target-oriented" capability of Kirchhoff migration is not possible with spectral or finite-difference migration methods. Kirchhoff image aliasing is only a problem from an aesthetic point of view, and when the migrated image is needed as input to subsequent multi-channel processing.

Operator aliasing occurs when the operator dip along the migration summation trajectory is too steep for a given input seismic trace spacing and frequency content. Spatial aliasing of Kirchhoff integral operators is likely because the operators are designed in the discrete space-time domain rather than the spectral domain. Great care must be taken to ensure that the f-k spectrum of a given space-time operator contains no aliased energy wrapped beyond the Nyquist frequency and wavenumbers. This implies that space-time operators which are spatially undersampled and contain significant steep-dip and high-frequency energy are likely to suffer from severe operator aliasing. In contrast, migration operators designed explicitly in the f-k domain are unaliased by definition, and operators designed in the f-x domain are easily modified to suppress spatial aliasing.

Previous work

Conventionally, anti-aliasing of Kirchhoff operators can be partially accomplished by trace interpolation, aperture control, and operator dip filtering. Trace interpolation de-

creases the spatial sample interval and thus increases the spatial Nyquist frequency, but at the potentially prohibitive cost of increasing the total 3-D migration input load (e.g., Yilmaz, 1988). Migration aperture control and operator dip filtering have the effect of suppressing aliased steep-dip contributions to the output image. Unfortunately, these suppressed steep dips may be precisely the events of interest when imaging near-vertical structure such as salt flanks and faults.

Hale (1991) proposed a method to anti-alias Kirchhoff dip-moveout (DMO) operators by replicating time-shifted versions of the input seismic traces to approximate a summation along an equal-time-sampled version of the operator. Hale's subsequent nearest-neighbor spatial interpolation implies a boxcar averaging of the input trace values along the time direction, whereas we use triangle filtering to increase accuracy at steep migration dips. Hale's test of summing DMO impulse responses and matching the result to the original impulse ensures both operator aliasing and image aliasing are suppressed, which may invoke more lowpass-filtering and loss of resolution than is strictly necessary for the case of migration operator anti-aliasing alone. Hale's replication of time-shifted input traces and spatial interpolations are inefficient from both a floating-point and memory perspective for 3-D migration algorithms, such as ours, that process thousands of traces simultaneously.

Gray (1992) proposed an approximate but cost-effective method to anti-alias Kirchhoff migration operators by performing aperture-dependent lowpass temporal filtering of the input trace data. He suggested that approximately three copies of the input data be lowpass-filtered at different high-cut frequencies. During migration the wide-aperture portions of the migration operator would be drawn increasingly from the lowest-frequency-content filtered trace copies. This corresponds to the notion that the wide-aperture portions of the migration operator have the steepest dips and therefore only the lowest frequencies will be unaliased. We more accurately calculate the complete vector of high-cut frequencies separately for each diffraction trajectory, and design and apply our anti-alias filters on the fly accordingly. Our method is as cost-effective as Gray's approach, but does not require the memory-intensive storage of multiple data copies to implement the anti-aliasing.

We present an improved method for anti-aliasing Kirchhoff migrations. We first derive the relevant operator aliasing criteria and then present our efficient method of anti-aliasing the migration operator by local triangle filtering of the seismic trace. Finally, we compare applications of our anti-aliased Kirchhoff migration to conventional aperture-weighted Kirchhoff migration on a 3-D marine seismic data example.

ANTI-ALIASING THEORY

The operator anti-aliasing criterion defines the maximum unaliased temporal frequency in the seismic data at the location that the operator trajectory intercepts a seismic trace, and is a function of the local operator dip and the trace spacing. In order to remain unaliased, the sequence of seismic trace samples summed along the operator trajectory must satisfy the dip Nyquist sampling criterion:

$$f_{max} \le \frac{1}{2\Delta T} = \frac{1}{2(\partial t_k/\partial \rho)\,\Delta \rho}. \qquad (1)$$

The factor ΔT is the moveout time along the migration operator between adjacent traces. The term $\partial t_k/\partial \rho$ is the local spatial derivative of the migration operator at the point of intersection with the seismic trace, and $\Delta \rho$ is the seismic trace spacing along the recording surface. The anti-aliasing criterion (1) suggests local lowpass filtering of the seismic trace to ensure that no frequencies larger than f_{max} are incorrectly migrated into the output image. As discussed later, we implement the anti-aliasing lowpass filtering efficiently and robustly with local triangle filters.

Kirchhoff time migration

It is instructive to evaluate the anti-aliasing criterion for the special case of Kirchhoff *time* migration, which can be extended to the case of Kirchhoff *depth* migration. For time migration, we derive an expression for the anti-aliasing criterion (1) by analytically evaluating the operator derivative term $\partial t_k/\partial \rho$. We begin by considering the analytic expression of the Kirchhoff 3-D prestack time migration operator, which has the form

$$t_k = t_s + t_r \approx \sqrt{\left(\frac{\rho_s}{v}\right)^2 + \tau^2} + \sqrt{\left(\frac{\rho_r}{v}\right)^2 + \tau^2}. \qquad (2)$$

The term t_k is the total two-way Kirchhoff migration reflection traveltime, τ is the one-way vertical traveltime or pseudo-depth to the reflection point, and v is the rms migration velocity that varies as a function of space and pseudo-depth (x, y, τ). The lengths ρ_s and ρ_r are the distances measured along the planar recording surface between the source or receiver, respectively, to the vertical projection of the image point on the recording surface, expressed as

$$\rho_* = \sqrt{(x_* - x_i)^2 + (y_* - y_i)^2}, \qquad (3)$$

Equation (3) assumes that the recording surface is a horizontal plane at a constant datum depth z_0. The subscript $*$ is a wildcard for either the source or receiver coordinate subscripts s and r, and the subscript i refers to the surface location of the subsurface image point projected up onto the recording surface.

The spatial derivative of (2) is needed to determine the migration operator aliasing criterion, which can be derived as

$$\frac{\partial t_k}{\partial \rho} = \pm\sqrt{\left(\frac{\partial t_k}{\partial x_i}\right)^2 + \left(\frac{\partial t_k}{\partial y_i}\right)^2} \approx \frac{1}{v^2}\left(\frac{\rho_s}{t_s} + \frac{\rho_r}{t_r}\right). \qquad (4)$$

We evaluate the effective rms spatial sampling interval $\Delta\rho$ for the prestack migration operator as

$$\Delta\rho \approx \sqrt{\frac{1}{2}(dx_s^2 + dy_s^2 + dx_r^2 + dy_r^2)} \qquad (5)$$

where we define dx_s and dy_s in the prestack case as

$$dx_s = \frac{|x_i - x_s|\Delta x}{\rho_s} \qquad (6)$$

and

$$dy_s = \frac{|y_i - y_s|\Delta y}{\rho_s} . \qquad (7)$$

The terms Δx and Δy are the true inline and crossline sampling intervals of the seismic trace data, and are assumed to be regular but possibly unequal in length. A more complicated analysis is required for irregular trace spacings, which this paper does not address.

Given the analytic expressions for the spatial derivative of the Kirchhoff time migration operator $\partial t_k/\partial\rho$, and the definition of the areal trace spacing interval $\Delta\rho$, we derive an analytic expression for the time migration operator anti-aliasing criterion. For the prestack case, the anti-aliasing criterion is

$$f_{max} \le \frac{v^2}{2\Delta\rho}\left(\frac{\rho_s}{t_s} + \frac{\rho_r}{t_r}\right)^{-1} , \qquad (8)$$

where the prestack definition of $\Delta\rho$ given by (5) – (7) must be used.

Kirchhoff depth migration

In contrast to the time migration method above, the depth migration anti-aliasing criterion does not have a general analytic solution. Kirchhoff depth migration operators in $v(x, y, z)$ media do not have simple hyperbolic forms, and must be evaluated numerically through heterogeneous migration velocity models. However, we propose three methods to provide satisfactory depth migration anti-aliasing results.

The first and most straightforward method is simply to use the rms velocity field v and the time migration anti-aliasing criterion (8), of the previous section, to design the anti-aliasing lowpass filters along the non-hyperbolic depth migration operators. This approach is robust because the dip along the time migration operator is a reasonable approximation to the *average* dip $\partial t_k/\partial\rho$ along the true depth migration trajectory.

The second depth migration anti-aliasing technique applies to Kirchhoff depth migration driven by traveltime tables. In this case, the operator derivative $\partial t_k/\partial\rho$ in the general anti-aliasing criterion (1) can be evaluated by differencing the source and receiver traveltimes at the trace location with respect to an adjacent source and receiver location. This approach is more accurate than the time migration approximation, but requires extra memory and I/O overhead to load the adjacent traveltime tables, or extra computation time if the adjacent traveltimes are interpolated from a sparse set of traveltime tables already loaded into memory.

The third depth migration anti-aliasing technique applies to Kirchhoff depth migration in which the traveltime values are computed by raytracing on the fly. In this case, an extra set of rays can be traced from adjacent source and receiver locations down to all subsurface points, or interpolated from a single set of dynamic rays by paraxial interpolation. Then the difference in ray arrival times can be used to approximate the operator derivative $\partial t_k/\partial\rho$ in (1). This method is more computationally intensive than the traveltime table approach, but has significantly smaller memory requirements.

In the sections that follow, we assume that the operator derivative $\partial t_k/\partial\rho$ of equation (1) is a known quantity, whether for time or depth migration, since it can be calculated by any of the three methods described above.

ANTI-ALIAS FILTER DESIGN

Given that we know the maximum unaliased frequency f_{max} at each point along the migration operator, we need to design a method to locally lowpass filter the seismic data in order to satisfy the anti-aliasing criterion (1). We implement the local lowpass filters as triangular smoothing. The $\mathcal{Z}$-transform representation of an arbitrary N-point triangle filter can be expressed as

$$g(z) = \frac{-z^{-k-1} + 2 - z^{k+1}}{\alpha(1 - z)(1 - z^{-1})} , \qquad (9)$$

where the triangle length $N = 2k + 1$, and the filter scaling coefficient $\alpha = (k + 1)^2$. The amplitude spectrum of the triangle filter can be derived as

$$A(\omega) = \frac{\sin^2(\omega\Delta t(k + 1)/2)}{\sin^2(\omega\Delta t/2)} , \qquad (10)$$

which is the discrete version of a continuous sinc^2 function, and has spectral notches at the frequencies

$$f_n = \frac{\omega_n}{2\pi} = \frac{n}{(k + 1)\Delta t} \quad ; \quad n = 1, 2, 3, \ldots . \qquad (11)$$

We design the triangle filter length N such that the maximum unaliased frequency f_{max} is equal to the first notch in the triangle spectrum at frequency f_1. Equating the anti-aliasing criterion (1) to the first triangle filter notch frequency of (11), we derive the appropriate anti-aliasing triangle filter length N to be

$$N \ge \max\left(4\left(\frac{\partial t_k}{\partial\rho}\right)\frac{\Delta\rho}{\Delta t} - 1 , 1\right) . \qquad (12)$$

The value of the local migration operator dip $\partial t_k/\partial\rho$ is given by equation (4) in the case of time migration, or by the methods discussed in the previous section on depth migration.

Furthermore, we note that the denominator of $g(z)$ represents a causal integration of the trace with $1/(1-z)$, followed by an anticausal trace integration with $1/(1-z^{-1})$. The numerator of $g(z)$ is a gapped three-point Laplacian operator, where the length of the gap $(k+1)$ determines the triangle length N and high-cut frequency f_{max}. Therefore, if the input trace data are integrated twice before migration, an arbitrary N-point anti-alias triangle filter can be designed and applied on the fly for the cost of a three-point operator. This observation offers a large savings in computational effort when applying the triangle filters.

DATA EXAMPLES

We compare our anti-aliased Kirchhoff migration to a conventional aperture-weighted Kirchhoff migration, both implemented on a Connection Machine CM-5. Preliminary 3-D results were shown by Lumley and Claerbout (1993). Figure 1 shows how our anti-aliasing method enhances a 3-D Kirchhoff migration image of a salt intrusion, given a sparse 50m-binned input dataset. We will discuss 2-D and 3-D data examples in more detail at the oral presentation.

CONCLUSIONS

We present an anti-aliasing method for Kirchhoff migration operators, based on local triangle filtering. The N-point triangles are efficiently applied as 3-point filters after causal and anticausal integration of the seismic trace data. This method is well suited for parallel processing algorithms, where storage of multiple copies of various high-cut filtered versions of the input data is not often practical. We compare the anti-aliasing method to a standard Kirchhoff 3-D migration, using a salt intrusion data set from the Gulf of Mexico.

Our results indicate that careful operator anti-aliasing can enhance steep-dip reflections from faults and salt-sediment interfaces during the process of 3-D seismic migration imaging. Our method is applicable to other Kirchhoff space-time operators such as NMO velocity stacking and DMO.

ACKNOWLEDGMENTS

We thank the Sponsors of the Stanford Exploration Project (SEP) and the SEP SuperComputing Tier members for supporting this research. Halliburton Geophysical Services kindly donated the 3-D salt intrusion dataset used in this study. We thank Dave Nichols, Biondo Biondi and Stew Levin for helpful comments on the subject of operator aliasing.

REFERENCES

Claerbout, J. F., 1992, Earth soundings analysis: Processing versus inversion: Blackwell Scientific Publications.

Gray, S. H., 1992, Frequency-selective design of the Kirchhoff migration operator: Geophysical Prospecting, 40, 565–571.

Hale, D., 1991, A nonaliased integral method for dip moveout: Geophysics, 56, 795–805.

Lumley, D. E., and Claerbout, J. F., 1993, Anti-aliased Kirchhoff 3-D migration: a salt intrusion example: Annual SEG Summer Research Workshop on 3-D Seismology, Soc. Expl. Geophys., Expanded Abstracts, 115–123.

Spitz, S., 1991, Seismic trace interpolation in the F-X domain: Geophysics, 56, 785–794.

Yilmaz, O., 1988, Seismic data processing: Soc. Expl. Geophys., Tulsa.

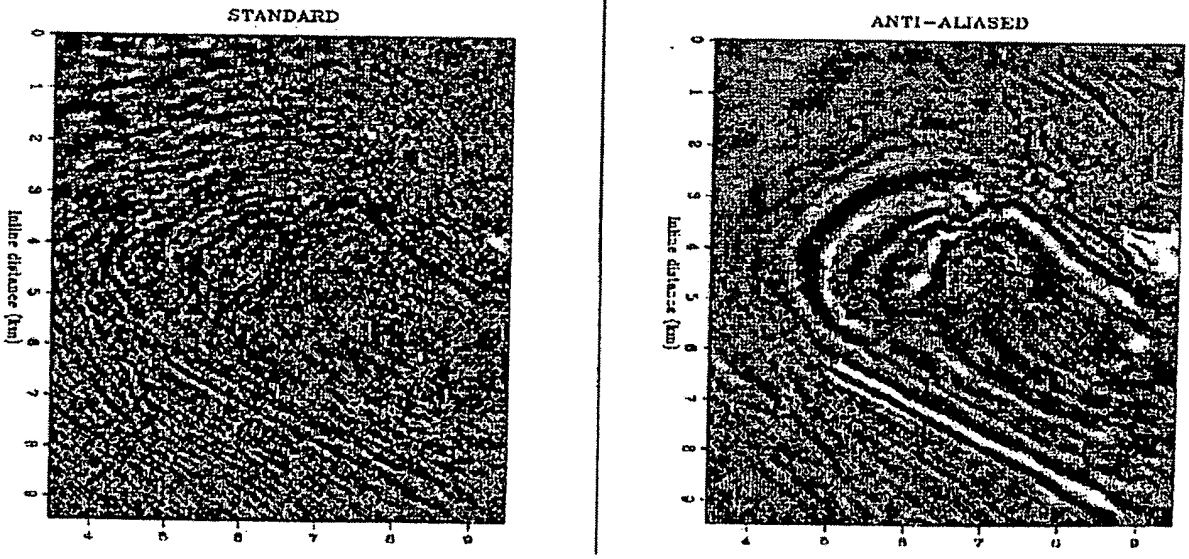

Figure 1: Kirchhoff 3-D migrated time slices at 1.744 seconds. The left panel is a standard Kirchhoff 3-D migration with a 60-degree migration aperture and $\cos^2\theta$ operator dip filter, the right panel is our new anti-aliased migration method.

Geophysical Prospecting 40, 565–571, 1992

FREQUENCY-SELECTIVE DESIGN OF THE KIRCHHOFF MIGRATION OPERATOR[1]

SAMUEL H. GRAY[2]

ABSTRACT

GRAY, S.H. 1992. Frequency-selective design of the Kirchhoff migration operator. *Geophysical Prospecting* 40, 565–571.

Integral migration techniques perform a sum over an aperture of input traces to obtain output at a single point. The length of the aperture is limited by a spatial Nyquist criterion, which typically prohibits imaging very steep dips at very high frequencies without generating severe migration artifacts (migration operator aliasing). For time-domain Kirchhoff migration, this can be a fatal shortcoming. The standard way to address this problem is to interpolate traces spatially before migration. This reduces the trace spacing, thereby increasing the frequency content which can be migrated without aliasing at steep dips.

An alternative remedy to the operator aliasing problem is to modify the phase response of the Kirchhoff migration operator. This operator is frequency-selective across the migration aperture: it passes all temporal frequencies of the input traces in the innermost portion of the aperture (referring to the shallow dips), and gradually cuts out the higher frequencies as it approaches the outer portion of the aperture. Thus, while all frequencies of the input data contribute to the shallow-dip portion of the migrated image, only the permissible low frequencies of the input data contribute to imaging the steepest dips.

Using a simple realization of a frequency-selective Kirchhoff migration operator, this technique is illustrated on a synthetic data set involving greater than vertical dips.

INTRODUCTION

For integral migration methods, a major advantage of working in the time domain rather than the frequency domain is speed, and a major disadvantage is inflexibility of the migration operator. In the frequency domain, the migration operator can be changed for each frequency, allowing for an optimal combination of steep-dip imaging accuracy and rejection of unwanted data. For example, the combination of steep dips, high frequencies and large CMP spacing presents no serious processing problems for integral migration performed in the frequency domain. For the lowest frequencies, the migration aperture can be unlimited; for the highest frequencies, the

[1] Received January 1991, revision accepted February 1992.
[2] Amoco Production Company, Research Center, P.O. Box 3385, Tulsa, OK 74102, U.S.A.

aperture must be limited by the need to exclude aliased data from the migration at steep dips. By contrast, time-domain integral migration is performed only once on a given section (not once per frequency), but the aperture must be limited to the worst-case frequency-domain migration aperture, namely the one used at the highest frequencies. Limiting the aperture in this way can result in the loss of a significant portion of the low-frequency steep-dip information in the migration. Not limiting the aperture can result in operator aliasing, which appears in the form of artifacts caused by migrating high-frequency data past their maximum allowable dip.

The most commonly applied solution to this problem, short of migrating in the frequency domain, is to interpolate the input seismic data to a finer spatial grid before migration. This results in an input section with smaller CMP spacing than the original section, and it increases the aliasing frequency for the migration according to the relation

$$\frac{f_{max}\,|\sin\theta|}{v(0)} \le \frac{1}{4\,\Delta x}, \tag{1}$$

where f_{max} is the maximum frequency retained in the data before migration, θ is the angle of emergence of a reflection event, $v(0)$ is the upper-surface acoustic velocity and Δx is the CMP spacing. This inequality is a statement of the Nyquist criterion for sampling, on the discrete grid of CMP locations, a continuous wave-field created by exploding reflectors in the earth: for each frequency f, unaliased transverse wavenumbers in the sampled wavefield ($2\pi f \sin\theta$ divided by half-velocity at the earth's surface) are limited in magnitude by $2\pi/2\Delta x$. To ensure that a Kirchhoff migration handles only unaliased input data, the Nyquist criterion must hold simultaneously for all temporal frequencies, so that f_{max} appears in (1). Attempting to migrate reflection data with temporal frequencies greater than f_{max} out to steep dips can result in artifacts which, in the worst case, might be interpreted as geological structure. Decreasing Δx increases the range of dips to which a given frequency component can be migrated; alternatively, it increases the range of frequencies which may contribute to a given dip in the image. Interpolating seismic data to decrease the CMP spacing, for the purpose of improving the migration operator response, requires an accurate interpolation routine (to avoid creating additional aliased data), and it increases the size of the data volume to be migrated, hopefully without creating new information. The cost of the interpolation is usually much smaller than the migration cost, and the added data volume increases the migration cost, though not usually to the point of being more expensive than a frequency-domain migration performed on the uninterpolated section. On a mainframe computer, the process of spatially interpolating a CMP section and then migrating using a time-domain integral method is often (but not always) an acceptable way to obtain a high-quality migrated section in 2D with a minimum of migration artifacts.

However, in 3D, multiplicative factors of two in computation and data storage costs can critically affect the choice of processing parameters for a post-stack migration. Target structures in 3D usually have their most rapid lateral geological variation in a preferred direction; this is usually the direction of choice for a single 2D

seismic line, and it usually defines the in-line, as opposed to cross-line, direction for a 3D survey. Current practice for 3D acquisition and processing calls for the grid spacing in the cross-line direction to exceed the grid spacing in the in-line direction, often by a factor greater than two. Premigration processing may be unaffected by this difference in spacings, but 3D migration can be affected dramatically. Therefore, in an attempt to make the migration grid isotropic and to minimize migration artifacts, data interpolation is often performed in the cross-line direction after stack and before migration.

The purpose of this note is to examine an alternative to data interpolation which can mitigate the problems of migrating seismic data with a large CMP spacing. This method is applicable to time-domain integral migration. (In frequency-domain integral migration, it is performed automatically). Because it does not require data interpolation, computation and data storage costs are reduced. Thus, the proposed method has the potential to allow 3D migrations on large data sets without compromising migration quality.

Modifying the Kirchhoff Migration Operator

Frequency-domain migration avoids operator aliasing by restricting the migration aperture when migrating the highest frequencies. In effect, this procedure ignores the portion of the input data with high transverse wavenumbers at high frequencies. A filter could be designed to perform this operation explicitly in the frequency-wavenumber domain before a time-domain migration, but the cost of the double Fourier transform and its inverse can be comparable to the cost of the spatial interpolation. Instead, the effect of the frequency-domain migration operator selection can be simulated very simply. Given an aperture suitable for migrating out to a specified maximum dip, the frequencies in the data which migrate out to the farthest offsets of the migration aperture are restricted and all frequencies which migrate out to the shorter offsets are left intact. Thus, the inner portion of a diffraction curve (Fig. 1) refers to the smallest dips. None of the frequencies in the seismic data are aliased for such small dips, so we can retain all the frequencies when migrating over that portion of the diffraction curve. On the other hand, the outer portion of the diffraction curve refers to the steepest geological dips, for which the highest frequencies present in the reflection events might be aliased. When migrating over this portion of the diffraction curve, only the lowest, unaliased frequencies may be retained. This requires a second copy of the input traces, containing no aliased frequencies. (The aliasing frequency can be computed from (1), using the angle of emergence of the ray which attains the steepest dip.) The third portion of the diffraction curve, referring to intermediate dips, should be migrated using a third copy of the input traces, whose high-frequency content is less than that of the original traces but greater than that of the second copy. If the migration proceeds by smearing out input traces onto the output section, rather than by summing along diffraction curves, the extra trace copies can be created, used and discarded along with each original input trace at almost no extra processing or storage cost. (In 3D migration,

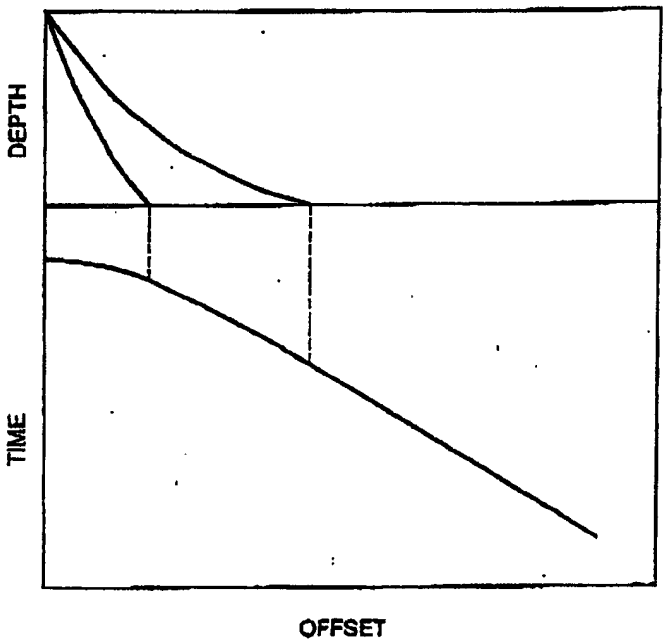

FIG. 1. Raypaths through a depth-varying medium, defining the portions of the diffraction curve for the various filtered versions of an input trace. The inner raypath, with the smaller take-off angle from the vertical, bounds the segment of the diffraction curve for which the input trace needs no reduction in high-frequency content. The outer raypath bounds the segment of the diffraction curve for which the input trace needs the most reduction in high-frequency content.

the basic unit of input data might be a block of several traces. This process then requires two extra blocks for a single block of original input traces, resulting in a non-trivial extra storage requirement.)

In its crudest form, the modified migration operator requires the creation of two or more extra copies of each input trace. The second copy has all the aliased frequencies removed, requiring a more severe high-cut filter than the one applied to the original traces. The third copy can be an average of the first two, retaining the highest frequencies at reduced amplitude. This approach yields a particular type of spatially-varying filter on the input traces which is analogous to some applications of time-varying temporal filters. That is, a time-varying filtered trace can be constructed by a weighted average, at every time sample, of several different band-pass-filtered versions of that trace; usually, lower-frequency versions are weighted more heavily at later times. Similarly, a spatially filtered set of input traces can be formed as weighted averages of a few band-pass-filtered versions of a single trace, with the lower-frequency versions being weighted more heavily at the largest offsets of the migration curve. Because the migration operator chooses a particular interpolated trace for mapping onto each offset, the procedure can be regarded as a migration operator interpolation.

The amount of aperture swept out by each of the (say, three) copies of an input trace is determined by the take-off angle of the ray sent from the trace location on the upper surface to the imaging location at depth. Figure 1 illustrates this. Raypaths with take-off angles obeying (1) with f_{max} of the original trace define the portion of the aperture swept out by the original trace, which has the greatest high-frequency content; this portion is limited to the small offsets. Similarly, the outer portion of the diffraction curve, determined by raypaths with the largest take-off angles specified by the migration program, requires a reduction of f_{max} in order to obey (1). The second copy of the input trace, which sweeps out the outer portion, will thus be the most severely high-cut version. The third copy of the input trace, which is an average of the first two, sweeps out the intermediate portion of the aperture. This copy of the trace can have a non-zero content of aliased frequencies, which can cause some problems when it sweeps out the farthest offsets of the intermediate portion of the migration aperture. Therefore, it may be desirable either to reduce slightly the maximum offset swept out by this trace copy or to perform a more sophisticated interpolation when sweeping out the intermediate offsets.

Yilmaz (1987, p. 324) mentions an alternative operator modification which is sometimes used. For the outer portion of the diffraction curve, more than one sample per trace is included for the summation which approximates the migration integral. Hale (1991) provides specific rules for applying this modification to integral dip moveout. This approach will have the same effect as the method proposed here (that is, it will perform the same spatial filtering operation on the input traces, resulting in the reduction of artifacts due to migrating aliased data). However, it is clearly more expensive to implement, since it adds operations to the most time-consuming part of the migration.

An Example

Figure 2 shows a finite-difference zero-offset synthetic seismogram from a salt dome with an overhung face. Acoustic velocities in the outlying sediments are typical for the Gulf of Mexico, allowing reflection energy from the overhung portion of the salt flank to turn upwards and be recorded. CMP spacing is 33 m and the maximum frequency present in the data is approximately 30 Hz. Figure 3 shows a turned-ray Kirchhoff migration of the input data, where no effort has been made to suppress the aliased frequencies at the steepest dips before or during migration. The migration was performed in depth and stretched back in time for display purposes. The steeply-dipping salt flank, including the overhung portion with a dip of 110°, has been well imaged, but the top part of the section is obscured by artifacts resulting from migrating the aliased frequencies. In fact, high-frequency data from the flat reflectors have been migrated to steep dips which obscure the image of the sediments. The steep-dip artifacts appearing inside and immediately above the salt dome result from migrating the myriad of steep-dip multiple reflection and reverberation events evident on Fig. 2; the modified migration operator is not designed to attack these. Figure 4 shows the modified Kirchhoff migration of the data, where the

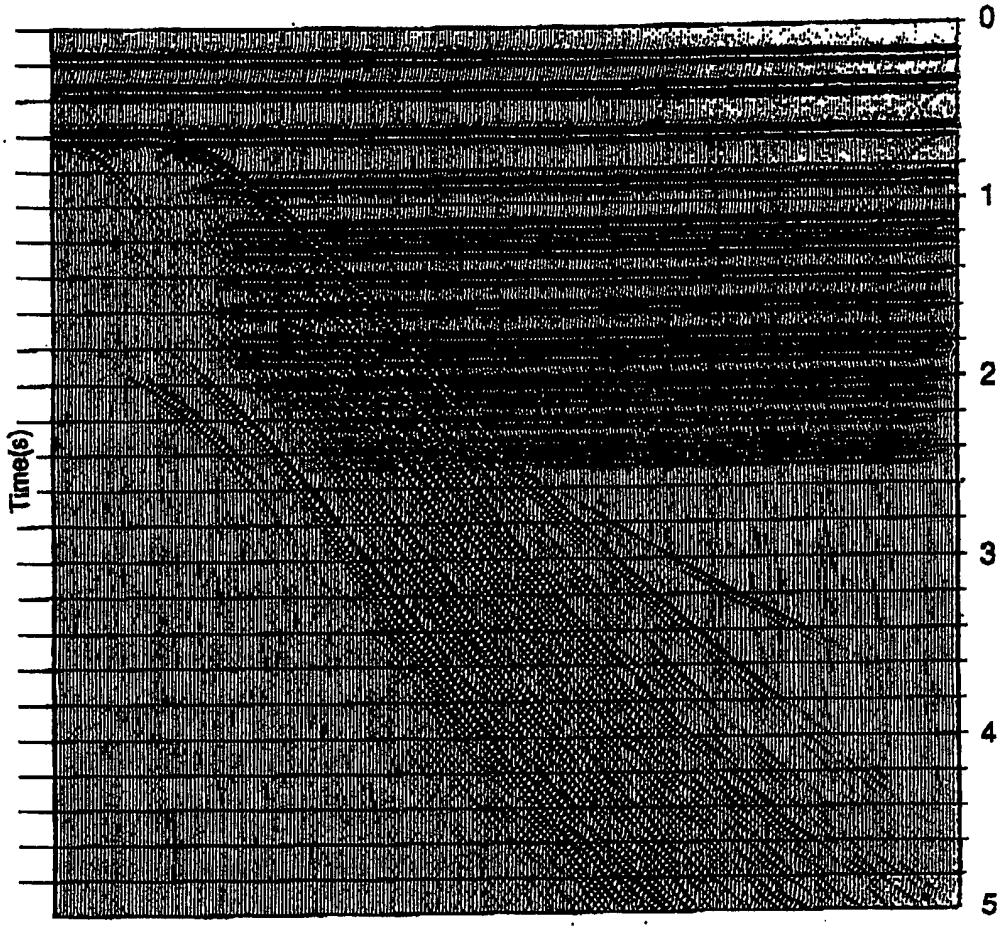

FIG. 2. Finite-difference zero-offset synthetic seismogram from a salt dome in a layered earth. The steepest dip is 110°.

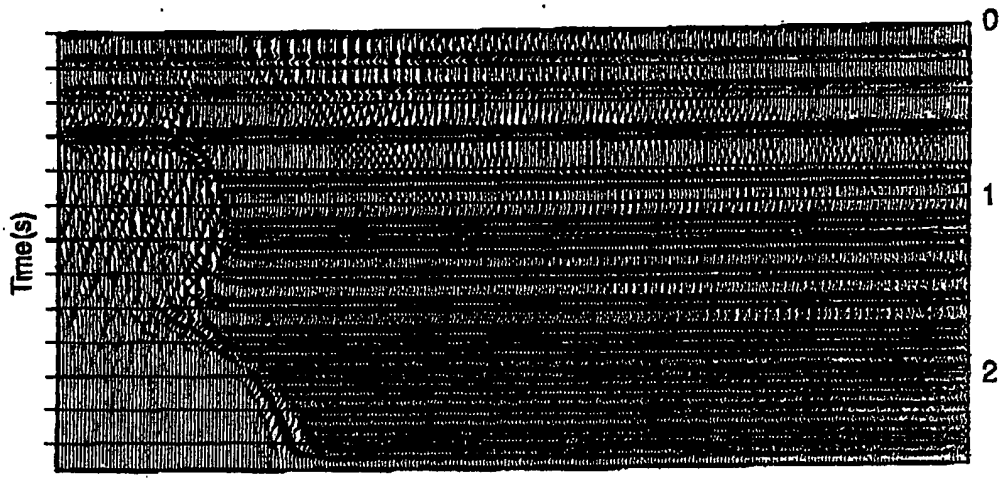

FIG. 3. Turned-ray Kirchhoff migration, with no attempt to suppress the aliased frequencies.

FIG. 4. Tu
resulting fr

migration
previous
artifacts
peared. I
reflectors

A techni
time-dom
and its re
technique
its diffrac
cated ray
sing is a
single-pas
sive and r

HALE, D. I
YILMAZ, O

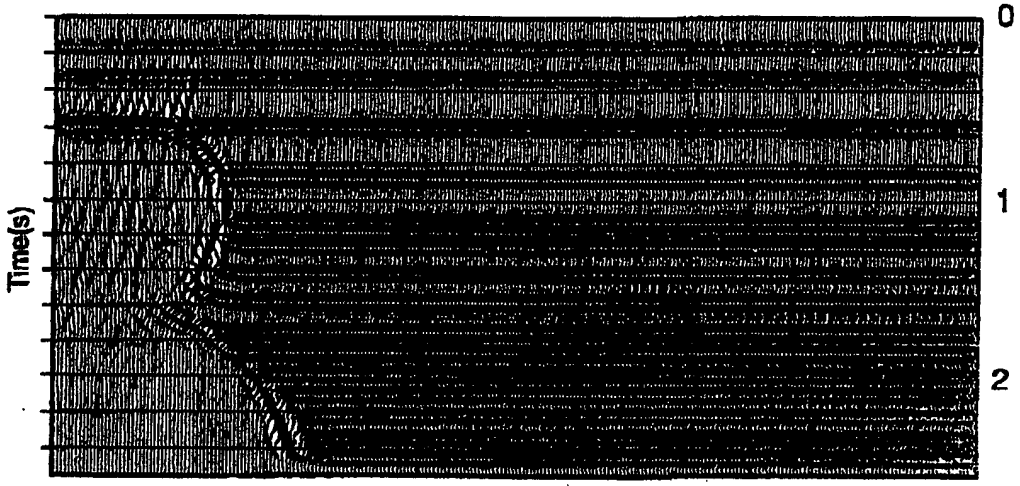

FIG. 4. Turned-ray Kirchhoff migration, using a frequency-selective operator. The artifacts resulting from migrating aliased data have been suppressed.

migration operator has been modified using the crude procedure described in the previous section. Figures 3 and 4 are scaled identically. As desired, the migration artifacts arising from migrating aliased frequencies have almost completely disappeared. In addition, there is no visible loss of high-frequency content on the flat reflectors relative to Fig. 3.

CONCLUSIONS

A technique has been proposed to eliminate one of the major disadvantages of time-domain Kirchhoff migration, namely the inflexibility of the migration operator and its resultant inability to image steep dips while including high frequencies. This technique is applicable both to time migration, which implicitly uses straight rays in its diffraction curve calculations, and to depth migration, which uses more sophisticated ray tracing. It is also applicable to integral dip moveout, where operator aliasing is a serious drawback. A major application should be in 3D migration, either single-pass or two-pass, where data interpolation presently serves as a fairly expensive and not entirely satisfactory alternative to migration operator aliasing.

REFERENCES

HALE, D. 1991. A nonaliased integral method for dip moveout. *Geophysics* 56, 795–805.
YILMAZ, O. 1987. *Seismic Data Processing*. Society of Exploration Geophysicists, Tulsa.

```
# Time Domain 15-degree Diffraction Movie
# Star:          w=p(t  ,z)       y=p(t  ,z+1)
# Star:          u=p(t+1,z)       v=p(t+1,z+1)
real p(36,96),u(36),w(36),v(36),y(36),e(36),f(36),d(36),z(96),alfa,beta
integer ix,nx,iz,nz,it,nt,kbyte
nx = 36;  nz = 96;  nt = 96;      kbyte=1
alfa = .125                  # v*dz*dt/(8*dx*dx)
beta = .140                  # accurate x derivative parameter; simplest case b=0.
open(3,file='plot40',status='new',access='direct',form='unformatted',recl=1)
do iz=1,nz;  do ix=1,nx;  p(ix,iz) = 0.                    # clear space
do iz=nz/5,nz,nz/4                                         # Set up initial model
        do it=1,15                                         # of 4 band limited
                do ix=1,4                                  # "point" scatterers.
                        p(ix,it+iz) = (5.-ix)*(8-it)*exp(-.1*(it-8)**2)
apb = alfa+beta; amb = alfa-beta                           # tridiagonal coefficients
diag = 1.+2.*amb;  offdi = -amb
do iz=nz,2,-2 {                                            # Climb up in steps of 2 z-levels
        do i=1,nz;  z(i)=0.;  z(iz)=1.      # Pointer to current z-level
        write(3,rec=kbyte) (z(i),i=1,nz),((p(ix,i),i=1,nz),ix=1,nx)
        kbyte = kbyte + nx*nz*4 + nz*4
        do ix=1,nx
                { u(ix) = p(ix,iz-1);          v(ix) = u(ix) }
        do it=iz,nt {
                do ix=1,nx        #update the differencing star
                        { w(ix) = u(ix);  y(ix) = v(ix);  v(ix) = p(ix,it) }
                dd = (1.-apb)*(v(1)+w(1))+apb*(v(2)+w(2))
                d(1) = dd-diag*y(1)-offdi*(y(1)+y(2))
                do ix=2,nx-1 {
                        dd   = (1.-2.*apb)*(v(ix)+w(ix))
                        dd   = dd + apb*(v(ix-1)+w(ix-1)+v(ix+1)+w(ix+1))
                        d(ix) = dd-diag*y(ix)-offdi*(y(ix-1)+y(ix+1))  }
                dd = (1.-apb)*(v(nx)+w(nx))+apb*(v(nx-1)+w(nx-1))
                d(nx) = dd-diag*y(nx)-offdi*(y(nx)+y(nx-1))
                call rtris(nx,diag+offdi,offdi,diag,offdi,diag+offdi,d,u,e,f)
                do ix=1,nx
                        p(ix,it) = u(ix)
                }
        }
do i=1,nz;  z(i)=0.;  z(1)=1.
write(3,rec=kbyte) (z(i),i=1,nz),((p(ix,i),i=1,nz),ix=1,nx)
stop;    end
```

FIG. 2.7-1. Time-domain diffraction movie program. (Clayton, Gonzalez, JFC, Hale)

Figure 2 shows the last frame in the movie produced by the test program. Exercise 1 suggests minor changes to the program of figure 1 to convert it from diffraction to migration. As modified, the program is essentially the original wave equation migration program introduced by Johnson and Claerbout [1971] and Doherty and Claerbout [1972].